Emergent Materials (2021) 4:1143–1165
https://doi.org/10.1007/s42247-021-00215-4

REVIEW

Metal oxide–grafted graphene nanocomposites for energy storage applications

D. Selvakumar[1,2] · P. Nagaraju[1,3] · M. Arivanandhan[1] · R. Jayavel[1]

Received: 8 January 2021 / Accepted: 5 April 2021 / Published online: 19 April 2021

Abstract
The graphene oxide and metal oxide–grafted graphene composites are studied on their promising electrochemical properties for high-performance supercapacitor applications. The identical decoration of metal oxide nanomaterials over the graphene structure reveals enhanced structural, thermal, and electrochemical stability to fabricate stable electrode materials. In the study, we review our recent studies on the utilization of graphene oxide and metal oxide–graphene grafted nanocomposites for energy storing applications.

Keywords Metal oxide–graphene · Nanocomposite · Energy storing applications · Supercapacitor

1 Introduction

Graphene is a single atom thick with self-possession of sp^2-intersected carbon atoms systematized on a honeycomb structure, the thinnest and strongest material turn into the intensifying material in material science owing to its remarkable physical properties as excellent structural, high surface area, electrical, mechanical and thermal characteristics [1–4]. Due to these unique properties, graphene sheets are prominently utilized in the supercapacitors [2–30], batteries [31], catalyst supports, nanoelectronics, and waste water treatment. Usually, the graphene oxide materials were produced by using modified Hummer's process with the normal graphite powder as a raw material. Graphene is reduced from graphene oxide (GO) by either of thermal treatment or chemical reduction [4]. Among them, the chemical method is predominantly preferred because of the low-cost process. During the oxidation of the graphite powder with acids and other oxidizing agents, the oxygen functional groups such as hydroxyl occupy the basal plane, whereas epoxyl, carbonyl, and carboxyl are decorated on the boundaries of GO layers [1, 4]. Among various reducing agents, thiourea is more effective due to less toxic. The assembly of metal oxide nanomaterials decorated on graphene layers reveals enhanced efficiency of energy devices due to the excellent electron accepting property of graphene and high surface area [8]. The rare earth metal oxide materials are mixed with graphene to form composite structures, which can improve the conductivity of rare earth metal oxides and bounds the agglomeration and restacking of graphene [13]. The high surface area of RGO is predicted to be responsible for enhanced exceptional electrochemical features because of the characteristic restriction of RGO restacking accumulated from the π–π interface. In addition, appropriate spacer material (metal oxides) requires to be interpolated in the RGO sheet, which prevents the aggregation of graphene layers [26]. The reduced graphene oxide (rGO)–based papers are formed from the evaporation-induced self-assembly of chemically produced graphene oxide, followed by thermal treatment [30]. By using the freestanding and flexible rGO papers, solid-state electronic devices such as flexible supercapacitors, actuators, solar cells, and ammonia sensors were fabricated with addition of impurities [32–35]. Because of the superior properties, graphene–metal oxide nanocomposites can be used in superior performance supercapacitors for efficient energy storage applications.

2 Experimental procedure

GO powder was formed with graphite materials through the modified Hummer's process. In the classic synthesis, 0.5 mol

✉ R. Jayavel
rjvel@annauniv.edu

[1] Centre for Nanosciennce and Technology, Anna University, Chennai 600025, India

[2] Research and Development Centre, Sri Krishna College of Engineering & Technology, Coimbatore 641008, India

[3] Department of Physics, School of Arts and Science, Vinayaka Mission Research Foundation, AV Campus, Chennai 603105, India

thiourea (reducing agent) was mixed with the above dispersion during the stirring process at 95 °C about 12 h to reduce the as-prepared GO [1]. In order to increase the conductivity, phosphorous was introduced in the GO sheet through electrochemical process [2] and subsequently boron by hydrothermal treatment [3]. For the preparation of composites, a stoichiometric amount of metal oxide precursor (separately) was mixed with the as-prepared GO dispersion in a teflon-wrapped autoclave and ramped at a constant temperature throughout the reaction (hydrothermal). The precipitate was formed in the autoclave was filtrated, washed in ethanol and dried out on a vacuum oven. The composite precipitates were heat treated at an elevated temperature to form rGO (graphene)–metal oxide nanocomposites. Cadmium acetate (0.05 mol%), thiourea (0.05 mol%), and copper acetate (5 and 10 wt%) were added in graphene oxide dispersion by stirring. The reaction was processed on 60 °C about 4 h under hydrothermal behavior and the final material was washed, filtered, and dried out at 60 °C [4].

The graphene–CeO_2 nanocomposite was prepared by simple sonication and stirring from the precursor solutions of CeO_2 and rGO [5]. The reduced graphene oxide (0.3 g) was sonicated about 3 h and 0.1 g $NbCl_5$ was mixed through stirring process. One hour later, 5 ml hydrazine hydrate was mixed and stirred about 3 h. The as-prepared solution mixer was shifted in a teflon-wrapped autoclave and ramped on 140 °C about 24 h [6]. A 0.01 M copper nitrate hexahydrate was liquefied with 100 ml of distilled water and mixed with 20 mg of GO followed by the addition of 5 ml hydrazine hydrate. The pH of the solution was altered with liquid ammonia; later, the solution mixer was shifted to a 120-ml teflon-wrapped autoclave and ramped on 180 °C about 12 h [31]. The RGO–ZnO composite was prepared by hydrothermal method in a teflon-wrapped autoclave on 150 °C about 12 h [7]. Thioacetamide was mixed with a 40-ml double-deionized water and 0.98 g ammonium heptamolybdate tetrahydrate ($(NH_4)6Mo_7O_{24}{\cdot}4H_2O$) was mixed by 0.38 g citric acid through constant stirring. With this solution, the synthesized 0.1 g GO dispersion material was mixed through ultrasonication and stirred about 30 min. Finally, the blended mixer was taken by a teflon-wrapped autoclave and ramped on 180 °C about 24 h [8]. TiO_2 and WO_3/graphene–based nanocomplex were produced by simple in situ microwave irradiation process [9, 10]. Hydrothermal reaction was used to synthesis RGO/V_3S_4 binary nanocomposite materials at high temperatures (100 and 180 °C) [11]. For the RuO/RGO composite, 0.311 g ruthenium chloride hydrate material was liquefied using a 40-ml double-deionized water with 0.288 g of citric acid and 0.1 g of GO was mixed by ultrasonication and stirring. The combined mixer was shifted on a teflon-wrapped autoclave and ramped on 180 °C about 24 h [12]. The Gd_2O_3–graphene (Gd_2O_3/G) nanocomposites was prepared by mixing appropriate amount of Gd_2O_3 and synthesized graphene in 100 ml of distilled water through ultrasonication and stirring process [13]. BiVO4/RGO hybrid nanocomposite was prepared by hydrothermal process by heating at 180 °C about 24 h [14].

For the preparation of CuO/RGO composite, 0.1 M copper chloride was added using GO through the stirring process with addition of 0.1 M NaOH and the blended solution was treated using a microwave oven on 850 W about 6 min [15]. Mn_3O_4/rGO nanocomposites were prepared by in situ sol-gel reduction method [16]. Ytterbium oxide–graphene (Yb_2O_3G) composite was prepared by mixing 99 mg yttrium oxide (99.9%) in 100 ml of water dispersion through ultrasonication and 1 mg of as-prepared graphene through stirring process [17]. For the preparation of $BiYO_3$/RGO nanocomposite, the graphene oxide (100 mg) was ultrasonically distributed in HNO_3 dilution about 30 min, and stoichiometric quantities of $Bi(NO_3)_3.5H_2O$, $Y(NO_3)_3.6H_2O$, and hexamine materials were mixed with 20 ml NH_4OH solution through constant stirring on 70 °C [18]. The Co3O4/graphene nanocomposite was synthesized through hydrothermal route with graphene oxide powder (0.2 g), $CoCl_2.6H_2O$ (10 mmol), and urea [$CO(NH_2)_2$, 25 mmol] positioned in an oven ramped on 105 °C about 12 h [19]. Graphene/Mn-MoO_4 nanocomposites were prepared by 0.791 g of $(NH_4)6Mo_7O_{24}).4H_2O$, 0.027 g of $Mn(CH_3COO)_2$, 0.19 g critic acid, and 0.1 g graphene oxide was taken with a teflon-wrapped autoclave and ramped on 180 °C about 24 h [20]. MoO_3/G nanocomposite was synthesized using 80 mg of graphene oxide, 0.1 M hexa-ammonium molybdate tetrahydrate ($(NH_4)6Mo_7O_{24}.4H_2O$), and 3 ml HCl solution in a microwave oven kept by 850 W about 5 min [21]. The reduced graphene oxide 0.3 g was mixed with distilled water and sonicated about 3 h. At that time, 0.1 g $NbCl_5$ was mixed on a teflon-wrapped autoclave and ramped on 140 °C about 24 h. Appropriate quantity of cerium oxide (CeO_2) was mixed with 100 ml of water through ultrasonication process, and 1 mg of reduced graphene was mixed in the above dispersion [22]. Vanadium pentoxide/graphene oxide (VO-G) nanofibers were produced using electrospinning process [23].

The mixture rGO/WO_3 nanocompound was produced by using hydrothermal method with GO (0.1 g), 2.6 g of $Na_2WO_4.2H_2O$ (0.1 M), and 0.48 g of NaCl (0.1 M) [24]. Composite PCMs (caprylic acid) were synthesized by adding 0.5 wt% ZnO, CuO, Ag, and GO nanoparticles with the caprylic acid PCM, distinctly with SDBS surfactant as the capping agent under the sonication process [25]. Of $Ce(NO_3)_3.6H_2O$ material, 2.17 g was mixed with GO and CNT dispersion solution and 10 mg of NaOH pellets were mixed with uphold the solution mixer at pH 10 under vigorous stirring for 6 h at 90 °C [26]. Of nickel (II) nitrate hexahydrate material, 1.163 g was mixed with GO/CNT dispersion solution using mechanical shaker (vortex mixer) about 5 min. As-prepared solution was then shifted to a teflon-wrapped

autoclave, ramped on 150 °C about 12 h to form RGO/CNT/NiO nanocomposite [27]. The RGO/Mn_2O_3:Co_3O_4 metal oxide nanocomposite was prepared by mixing cobalt chloride monohydrate ($CoCl_2 \cdot H_2O$) and manganese chloride monohydrate ($MnCl_2 \cdot H_2O$) of weight ratio as 7:3 (1 g) mixed with the dispersed RGO and stirred continuously using an oil bath on 60 °C about 30 min [28]. In_2O_3/CNT/RGO nanocomplex was prepared using 50 mg of dispersed GO in N, N dimethylformamide and water (3:1 v/v, DMF:H_2O, 80 mL) mixture with the addition of CNT (25 mg) and $InCl_3$ (75 mg) [29]. The facile preparation of reduced GO paper was realized through evaporation-induced self-assembly process [30]. Dopants were incorporated to prepare composite rGO paper for effective electrode material in the solid state electronic devices [32–35].

3 Results and discussion

3.1 Electrochemical properties of rGO

The electrochemical characteristics of the as synthesized composite electrodes were analyzed by using CV measurements using three-electrode systems with 1 M H_2SO_4 aqueous solution of the potential ranging of 0.1 to 0.9 V as revealed in Fig. 1. The CV arcs of GO illustrate a minor bulge and short current density in contrast to the rGO (Fig. 1(a)). The functional groups existing over the surface of GO show a vital part in an electrochemical action. Nevertheless, rGO arc illustrates that the current density improved over a greater integral space related to GO. A couple of poor redox plots were detected in place of rGO owing to the shift among the quinone/hydroquinone functionalities in carbon-based constituents. It offers an indication for the fractional existence of persistent oxygen enclosing functionalities over the exterior of rGO is energetic for Faradaic process. Figure 1(b and c) illustrates the arcs of the CV electrodes studied upon various sweep rates of GO and rGO materials. The CV performance differs through diverse sweep rates in growing integral range. The specific capacitances for the GO and rGO materials are computed from the integral area in the CV arcs and revealed in Fig. 1(d). The specific capacitance of the rGO material is considerably greater as compared with the GO at an equivalent sweep rate. For example, rGO material may extent 821.4 Fg^{-1} on a sweep rate on 10 mV/s, and it is approximately 4.7 periods higher than GO (172.7 Fg^{-1}). Once the sweep rate is improved as 20 mV/s, the calculated (specific) capacitance for rGO is 386.7 Fg^{-1} (roughly 47% those in 10 mV/s) [1]. The phosphor-doped graphene nanosheets possess 290 F g^{-1} as a specific capacitance on 0.5 A g^{-1} of current density by higher energy density as 43.75 Wh kg^{-1} [2]. In addition, the maximum specific capacitance of hydrothermally prepared boron grafted graphene nanosheets (HB-GNS) and thermally prepared graphene nanosheets (T-GNS) are 113 F/g and 52 F/g in 1 A/g of current density, correspondingly. The HB-GNS supercapacitor provides higher energy density (ED) ranging between 5.96–4.64 Wh kg^{-1} and 0.16–0.97 kW kg^{-1} as power density (PD) [3]. However, the electrochemical properties of CdS/rGO and $Cd_{1-x}Cu_xS$/rGO nanocomposite composites analyzed on a sweep rate as 50 mV/s indicate that the rise in electrochemical current for Cu-doped composite related to CdS/rGO composite [4].

3.2 Electrochemical properties of binary metal oxide-rGO nanocomposites

3.2.1 Graphene-CeO_2 nanocomposites

The specific capacitance for pristine CeO_2 and CeO_2G (CeO_2 and graphene nanocomposites) with varying quantities of graphene at dissimilar sweep rates are studied using cyclic voltammetry. Figure 2 illustrates the CV plots of (a) pure CeO_2, (b) CeO_2G1, (c) CeO_2G3, and (d) CeO_2G5 nanomaterials in a 1 M H_2SO_4 aqueous electrolyte. As revealed from Fig. 2(a), the pristine CeO_2 material exhibits capacitive behavior. As related to other electrode materials (Fig. 2(b) and (c)), the CeO_2G5 materials established the maximum current output through an observable double-layer current in the voltage ranging of −0.3 to +1.0 V, which is displayed in Fig. 2(d). The cyclic voltammogram at a fixed scan rate for pure and nanocomposites plotted in Fig. 2(e) demonstrates the dual-layer current reaction was enriched for the nanocomposite. The calculated specific capacitance for the CeO_2G5 nanocomposite perceived on 10 mV s^{-1} with a sweep rate of 109 F g^{-1}, related to CeO_2G1 nanocomposite (87 F g^{-1}) and pristine CeO_2 (75 F g^{-1}). The precise energy for the CeO_2G5 nanocomposite was 92.1 Wh kg^{-1}, approximately three times greater when compared to pristine CeO_2 (33.13 Wh kg^{-1}) [5].

3.2.2 Graphene–Nb_2O_5 nanocomposite

The 1st and 150th cycle of Nb_2O_5 nanoparticle cyclic voltammetry (CV) arcs on 100 mV s^{-1} sweep rate with the potential ranging of −1.5 V to +1.5 V are revealed in Fig. 3(a). The CV arcs of the 1st cycle and 500th cycle for rGO–Nb_2O_5 nanocomposite on 10 mVs^{-1} sweep rate are revealed in Fig. 3(b). The corresponding oxidation and reduction curves are obviously perceived. Fig. 3(c) displays the CV arcs for rGO, Nb_2O_5, and rGO– Nb_2O_5 nanocomposite materials on 100 mV s^{-1} sweep rate. The anodic current plot detected at −1.03 V for rGO–Nb_2O_5 nanocomposite material is ascribed to Li+ extraction. CV analysis of rGO–Nb_2O_5 nanocomposite materials executed at various sweep rates (such as 10, 20, 30, 40, 50, 100, 150 mV s^{-1}) through lithium perchlorate electrolyte express the superior

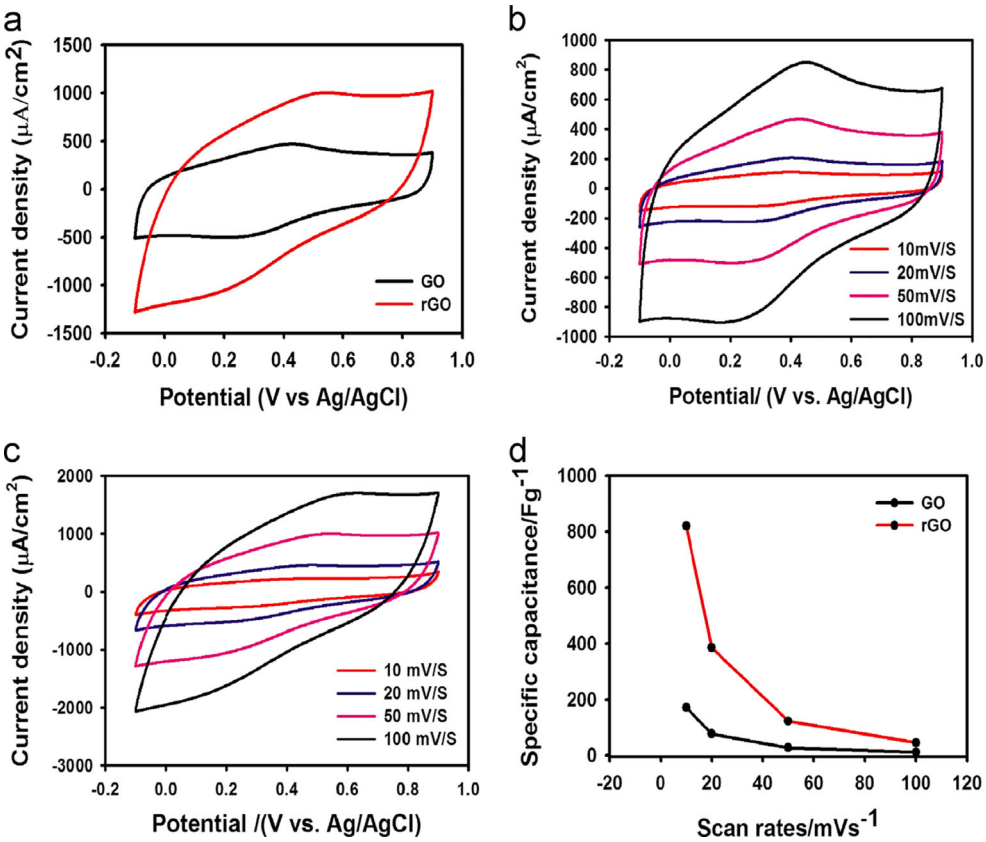

Fig. 1 Cyclicvoltommogram arcs for the GO and rGO in 1 M H_2SO_4 aqueous solution. **a** Relative CV arcs for the GO and rGO nanomaterials on a sweep rate as 50 mV s^{-1}, **b** CV arcs of GO nanomaterials on various sweep rates, **c** CV arcs for rGO nanomaterials on various sweep rates, and **d** computed specific capacitance on diverse sweep rates for the GO and rGO nanomaterials

electrochemical reversibility characteristics as revealed in Fig. 3(d). The specific capacitances are calculated through succeeding relation from the CV graph.

$$C_s = \int \frac{IdV}{vmV}$$

while I is output current, V is voltage, v is sweep rate, and m is mass of the nanocomposite materials over the electrode surface. The calculated specific capacitance as 321 Fg^{-1} attained on 10 mV s^{-1} sweep rate for the rGO–Nb_2O_5 nanocomposite. The calculated specific capacitance in the current study is comparable with the literatures. The calculated specific capacitance (Cs) at different sweep rates (such as 10, 20, 30, 40, 50, 100, and 150 mV s^{-1}) exists as 321.2, 290.6, 226.5, 201.5, 177.9, 80.6, and 72.1 Fg^{-1} consistently. The cyclic constancy for the graphene–Nb_2O_5 nanocomposite maintains 91% of its original capacitance after 500 cycles and establishes an outstanding stability with higher reversibility of the material throughout the cycling test [6].

3.2.3 Graphene–CuO nanocomposite

The CV scans of CuO nanoparticles are presented in Fig. 4. The voltage ranging of −1.5 V to +1.5 V demonstrates that the oxidation of CuO to CuO + OH and the reduction from CuO to Cu_2O and Cu_2O to Cu peaks, respectively. The potential sweep of graphene and rGO–CuO nanocomposites in 100 mV/s illustrates the reversible cyclic behavior and large pseudocapacitance. The cathodic peak for 1.02 V is owing to the development of multi-step electrochemical response in the electrode among rGO–CuO and lithium ion development of $Li_2O_{0.18}$. The reverse reduction of Li_2O to lithium ions is recognized by the peak existing at 0.86 V. The nanocomposite demonstrates the oxidation peaks of CuO to CuO + OH, Li to Li_2O, and the reduction peaks of Cu_2O from CuO, Li from Li_2O shown in Fig. 5. The capacity diminishing of the rGO–CuO nanocomposite is very smaller after 100 cycles of charging and discharging, which will be acting as the potential material for storage systems [31].

3.2.4 Graphene–ZnO nanocomposite

The electrochemical studies of as-synthesized zinc oxide (ZnO), GO, and zinc oxide–graphene nanocomposite are examined using cyclic voltammetry. The inclusion of graphene improves the specific capacitance as well as electrochemical stability for metal oxides as reported in the literature. On the other hand, there is a synergistic effect maintained among the graphene and metal oxide. Figure 5(a) displays the CV arc in

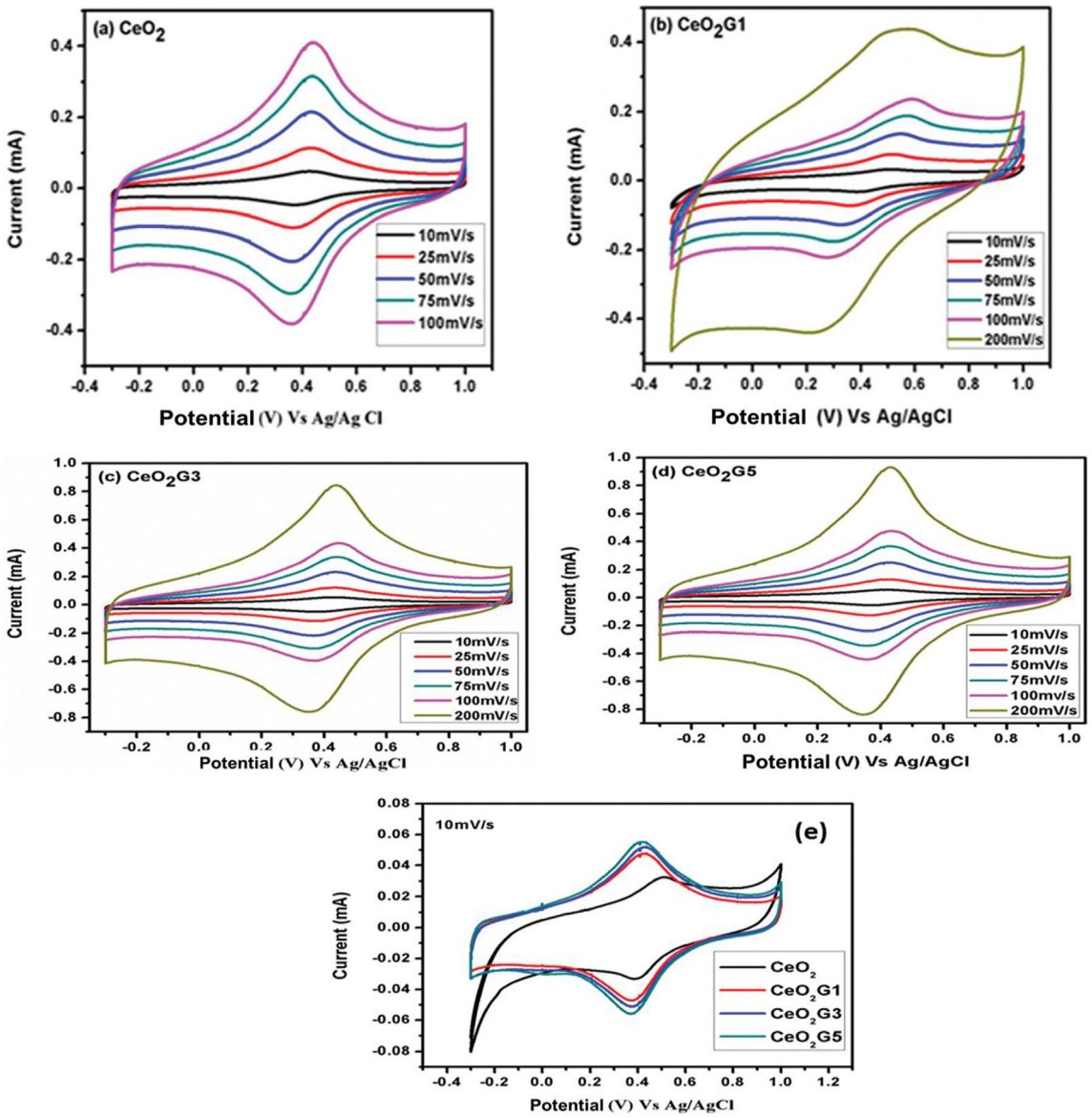

Fig. 2 Cyclic voltammetry plots for **a** pristine CeO_2, **b** CeO_2G1, **c** CeO_2G3, **d** CeO_2G5 nanomaterials for diverse sweep rates, and **e** comparative CV plots for pure CeO_2, CeO_2G1, CeO_2G3, CeO_2G5 on a sweep rate as 10 mV s^{-1}

the voltage ranging of 0.0 to 0.6 V with Ag/AgCl in the ZnO with sweep rates as 5 to 100 mV/s and detected by raising the voltage. Figure 5(b) illustrates the CV arc of GO nanomaterials. A quasi-rectangular form beside the current voltage axis is shown as lacking of noticeable redox humps. The results illustrates that whole sample possesses ideal capacitive performance in the sweep rates as 5 mV/s to 100 mV/s. Figure 5(c) demonstrates the CV arc for graphene–zinc oxide nanocomposite specifying an outstanding capacitance performance, small equivalent series resistance (ESR), and higher transmission for electrolyte ions in the nanocomposite and possess distinctive electric dual-layer performance through the rectangular edges. Apparently, the ZnO/GO materials reveal precise wide redox plot in the studied voltage region, indicates a characteristic reversible redox process for ZnO, and the region adjacent to CV arc is enriched through the ZnO material inclusion over the graphene edges. The Faradic curve for ZnO materials retain close symmetric with a minor curve parting, which indicates a better reversible and higher charge transfer procedure on the exterior restrained redox process. The superior voltammetry current in zinc oxide–graphene nanocomposite predominantly arises as of the pseudocapacitance for ZnO and moderately due to the electric dual-layer capacitance from graphene [7].

3.2.5 Graphene–MoS_2 nanocomposite

Figure 6 displays the CV graphs for pristine MoS_2, GO, and G/MoS_2 nanocomposite materials through the sweeping

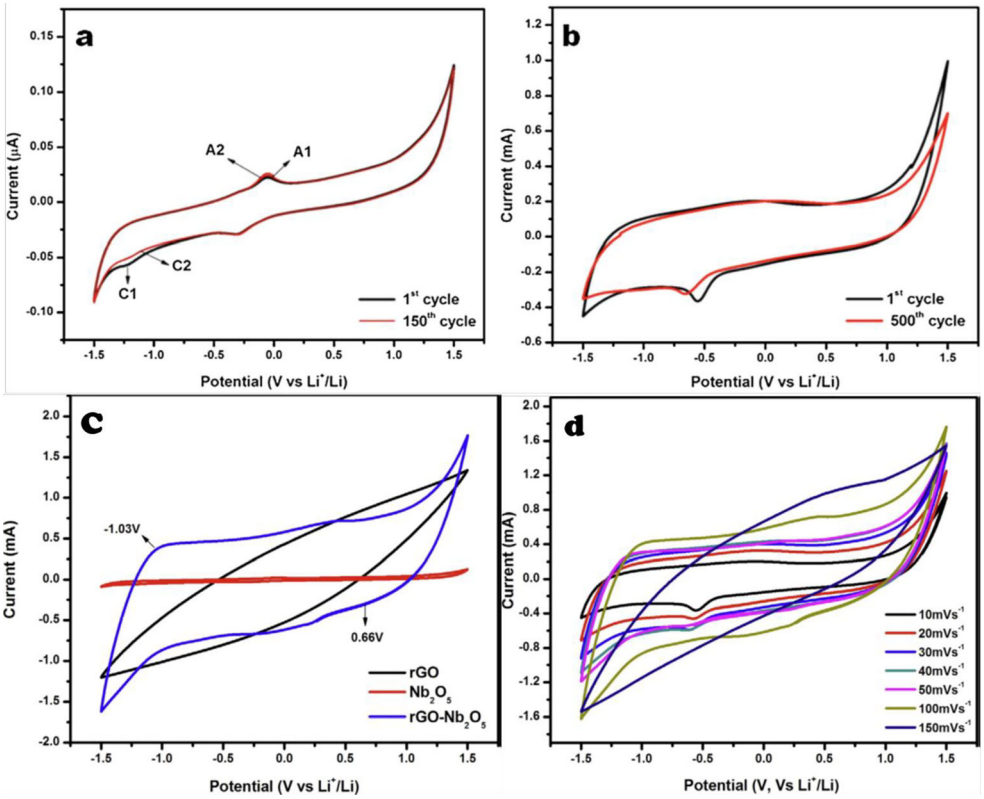

Fig. 3 CV arcs of **a** Nb_2O_5 for 1st and 150th cycle on 100 mV s^{-1} sweep rate; **b** rGO–Nb_2O_5 nanocomposites for 1st and 500th cycle on 10 mV s^{-1} sweep rate; **c** rGO, Nb_2O_5 and rGO–Nb_2O_5 nanocomposite materials on 100 mV s^{-1} sweep rate; **d** rGO–Nb_2O_5 nanocomposites on various sweep rates

speed of 1 to 100 mV s^{-1} with a potential from −0.8 to 0.6 V using 1 M aqueous Na_2SO_4 electrolyte. The zone in the CV graphs for the G/MoS_2 (0.1 g GO) material is greater compared with pristine MoS_2 nanoflacks with additional concentration of GO, pristine MoS_2, and lesser of GO materials, signifying an advanced precise capacitance with the synergetic influence of GO and MoS_2. However,

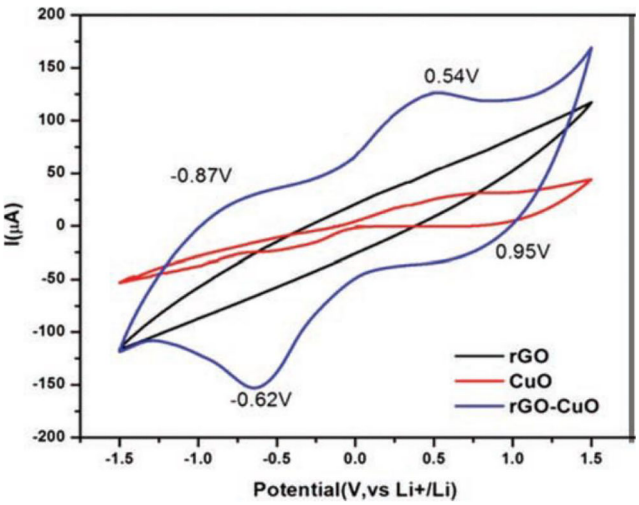

Fig. 4 CV scans of rGO, CuO, and rGO–CuO nanocomposite materials at a sweep rate as 100 mV/s

the capacitance properties for pristine GO or G/MoS_2 nanocomposite materials vary as of the electric dual-layer capacitance and the graphs near the rectangular profile through pseudocapacitance. As demonstrated in Fig. 7(a), the charging and discharging phase shows that the charge arc for 0.1 g GO in G/MoS_2 nanocomposites are nearly symmetrical with the consistent discharge correspondent having a minor curving points to better reversibility of the mixture constituents. The computed precise capacitances for the nanocomposite are 270, 240, 180, 155, 126, and 90 F g^{-1}, and on 0.1, 0.2, 0.3, 0.5, 0.7, and 1.0 A g^{-1} discharge current densities, correspondingly. The 0.1 g GO in G/MoS_2 nanocomposites reveal advanced specific capacitances (270 F g^{-1} on 0.1 A g^{-1}) on indistinguishable current densities than that for the G/MoS_2 nanocomposite with lesser GO concentrations, pristine MoS_2 nanoflacks (162.5 F g^{-1}) and GO, and greater related to preceding literature values [8].

3.2.6 Graphene–TiO_2 and graphene–WO_3 nanocomposite

The calculated specific capacitance (SC) for TiO_2/graphene nanocomposites from the chronopotentiometry arcs (Fig. 8) are 585, 376, 310, 284, and 265 Fg^{-1} on the current densities as 1, 2, 3, 4, and 5 Ag^{-1} correspondingly. The specific capacitance values of TiO_2/graphene materials were greater than pure TiO_2 materials. The specific capacitance retention and

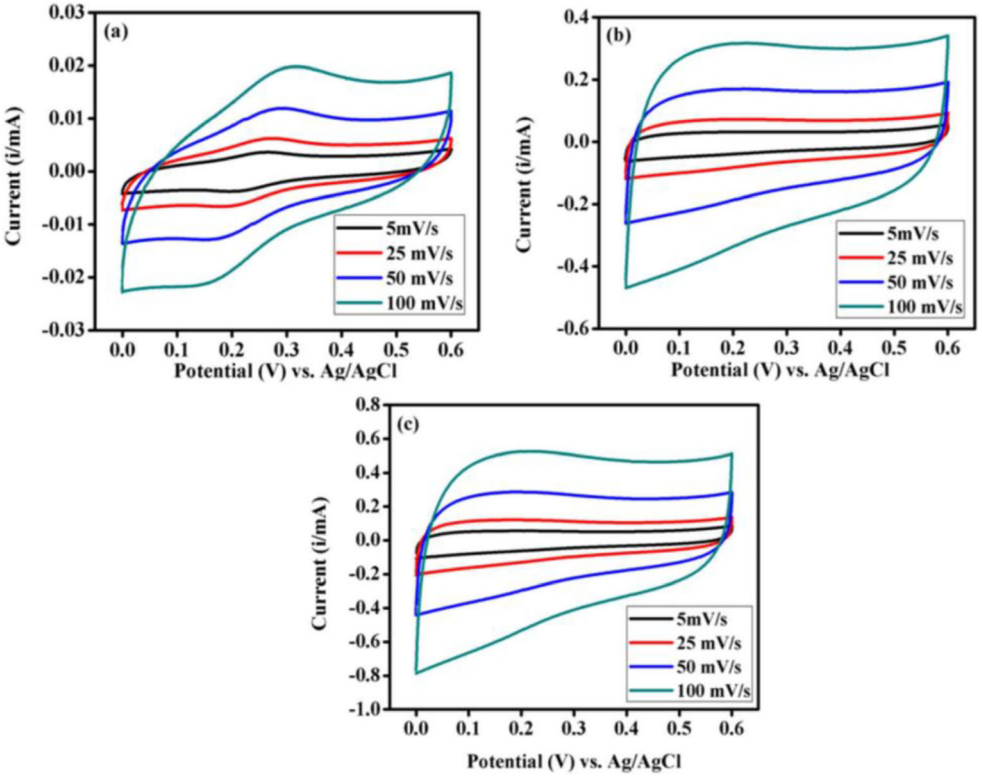

Fig. 5 Cyclic voltammetry arcs of **a** zinc oxide (ZnO), **b** graphene oxide (GO), and **c** zinc oxide–graphene composite at various sweep rates.

Columbic efficiency of the TiO_2/graphene materials offered 100% and 99.8 on 5000 cycles, signifying that nanocomposite material shows an improved cyclic stability. Outstanding supercapacitive enactment through great cyclic constancy because of the synergic influence on 3D TiO_2 nanomaterials and 2D graphene flack [9]. The SC of WO_3/G electrode material

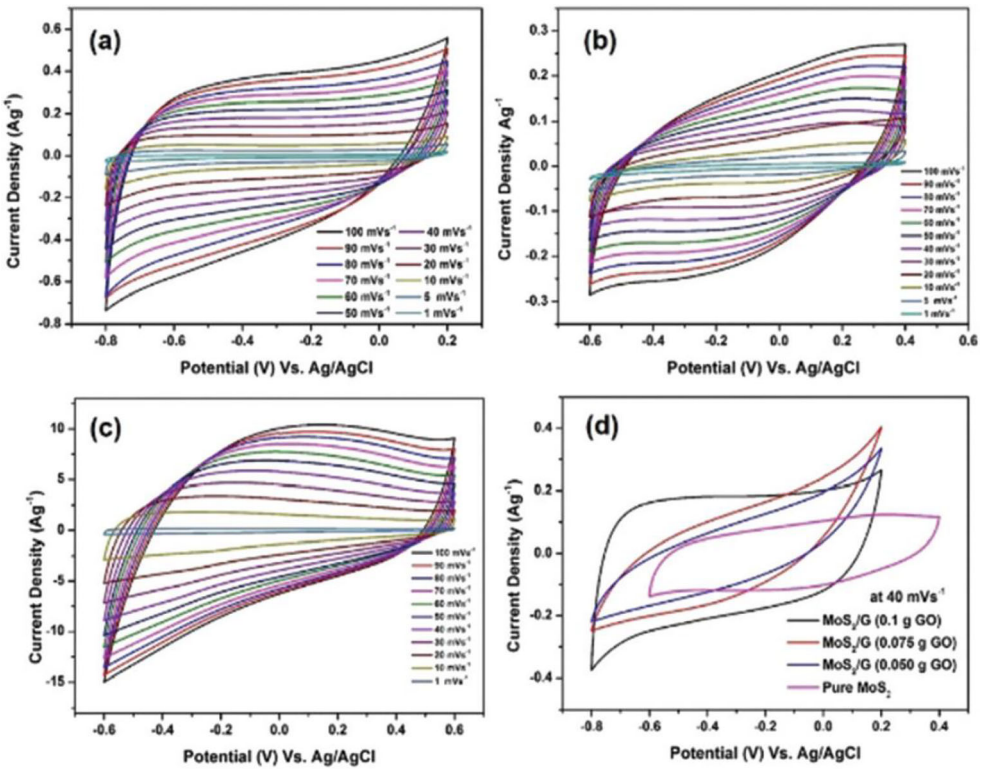

Fig. 6 CV graphs of **a** G/MoS_2 nanocomposite, **b** pristine MoS_2, and **c** graphene oxide nanomaterials on various sweep rates (such as 1, 5, 10, 15, and 100 mV s^{-1}) using 1 M aqueous Na_2SO_4 and the relation for all the data with a sweep rate on 40 mV s^{-1}

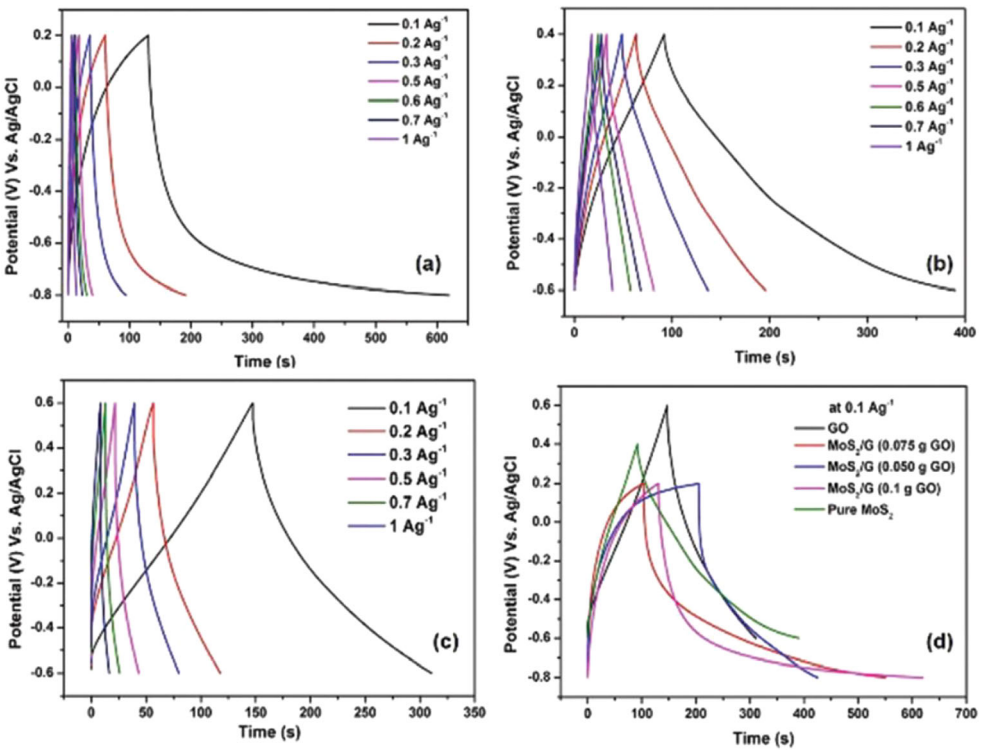

Fig. 7 Galvanostatic charge/discharge graphs for **a** G/MoS_2 nanocomposite, **b** pristine MoS_2, and **c** GO on various current densities (such as 0.1, 0.2, 0.3, 0.5, 0.7, and 1 A g^{-1}), **d** evaluation for all the data with a current density on 0.1 A g^{-1}

was calculated to be 761 Fg^{-1} on a current density as 1 Ag^{-1}. The nanocomposite material retains greater specific capacitance because of the porous arrangement that offers a great specific surface profile and slight interaction among WO_3 and graphene flack and assist earlier electron transport primary for superior capacitance. As a result, the greater surface profile and surface active-sites improve the ion dispersion, charge transmission and specific capacitance for nanocomposite materials [10].

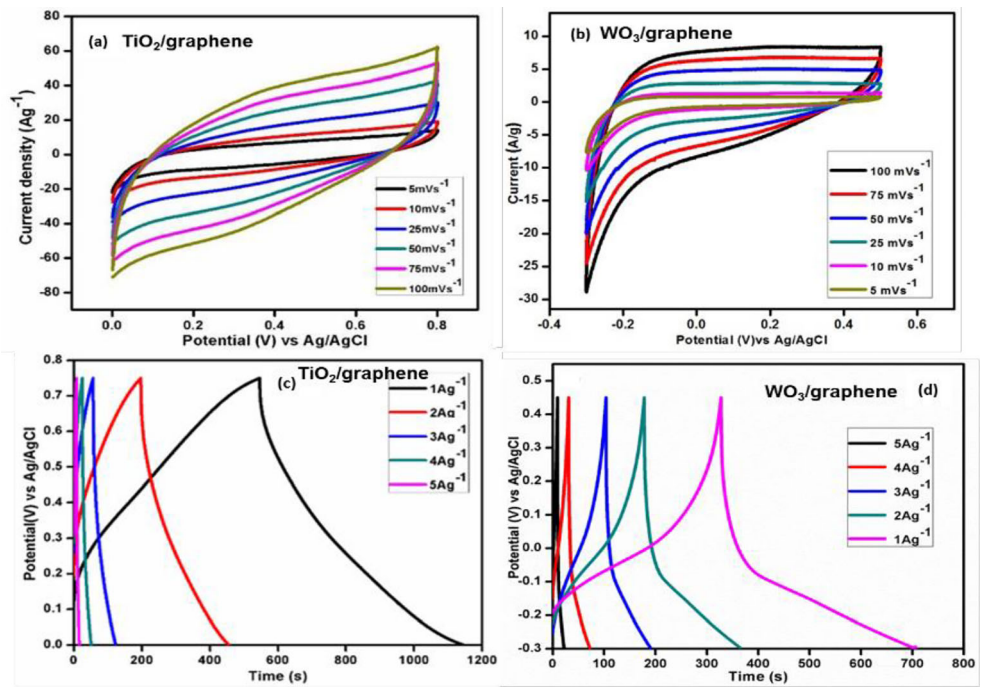

Fig. 8 CV arcs for **a**, **b** TiO_2/graphene and WO_3/graphene nanocomposite material on various sweep rates, **c**, **d** CP arcs for TiO_2/graphene, and WO_3/graphene material on various current densities

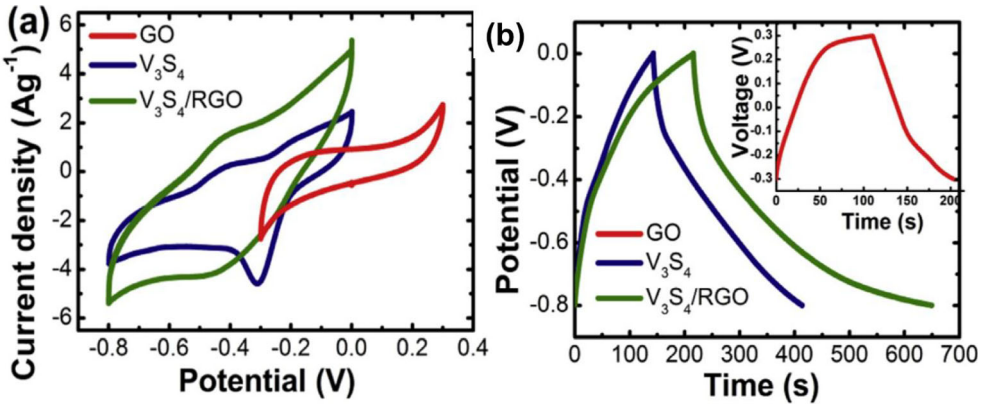

Fig. 9 Electrochemical supercapacitive characteristics of GO, V_3S_4, and V_3S_4/RGO adapted electrode materials: **a** CV arcs on 5 mV/s, **b** CD arcs on 1 A/g

3.2.7 Graphene–V_3S_4 nanocomposite

Figure 9(a) illustrates the CV arcs of pristine GO, pristine V_3S_4, and V_3S_4/RGO nanocomposites at a stable cycle rate on 5 mV/s. The calculated specific capacitance are 202 F/g (pristine GO), 318 F/g (pristine V_3S_4), and 500 F/g (V_3S_4/RGO nanocomposite). The CD arcs revealed in Fig. 9(b) relate charge-discharge of pristine GO, pristine V_3S_4, and V_3S_4/RGO nanocomposite through a working potential ranging from 0.0 to −0.8 V (for GO) and 0.3 to −0.3 V (V_3S_4 and V_3S_4/RGO) on the static current density as 1 A/g. From CD arcs, the calculated specific capacitance are 152 F/g (GO), 306 F/g (V3S4), and 520 F/g (V_3S_4/RGO). The V_3S_4/RGO nanocomposite illustrates an exceptional cyclic stability of 99.6% capacitance withholding, which is perceived at subsequent 2000 charge–discharge phases and signifies that the potential electrode material for applications in energy storage field [11].

3.2.8 Graphene–RuO_2, graphene–Gd_2O_3, and graphene–$BiVO_4$ nanocomposite

The RuO_2/G nanocomposite produces 441.1 Fg^{-1} as a specific capacitance at 0.1 Ag^{-1}, and there is a capacitance degradation of 6% subsequent 1000 rounds and reveals that the nanocomposite's outstanding cycle constancy [12]. Later, the rare earth metal oxide materials are mixed with graphene to form composite samples, which can improve the conductivity of rare earth metal oxides and inhibit the aggregation and restacking of graphene. Moreover, the nanocomposites also reveal a better electrochemical-activation property and significantly influence the electrochemical performance. Cyclic voltammetry studies of Gd_2O_3-G (5%) nanocomposite revealed 26 Fg^{-1} as the specific capacitance and greater than of pristine Gd_2O_3 (18 Fg^{-1}) [13]. Cyclic voltammetry and chronopotentiometric analysis of $BiVO_4$/RGO hybrid nanocomposite structure revealed 484 Fg^{-1} as the specific capacitance on a sweep rate as 5 mV s^{-1} and 343 Fg^{-1} on current density as 1 Ag^{-1} along with 87% for cycling constancy of the primary capacitance at subsequent 2000 charge/discharge rounds on 10 A g^{-1} [14].

3.2.9 Graphene–Cu_2O nanocomposite

The electrochemical studies of pure Cu_2O/graphene and Cu_2O/graphene nanocomposite was examined and displayed in Fig. 10. Figure 10(a) displays the CV plots for Cu_2O/G nanocomposites at several sweep rates and revealed a closely rectangular profile with supreme capacitive performance without a little distortion on an advanced sweep proportion as 100 mVs^{-1}. The region in the CV plots improved by raising the sweep rate holding the rectangular shape at respective sweep rates with high irreversibility at higher sweep rates. Figure 10(b) shows the charge-discharge plots of Cu_2O/G nanocomposites electrode materials with highest capacitance among all examined electrode materials through good rate competence. Higher capacitance with lesser IR drop is ascribed to the enhanced electrical conductivity on graphene through a conductive scheme of the Cu_2O nanoparticles play a major portion in charge transfer procedure. The nanocomposite material displays a greater capacitance because of Cu_2O grafted on the surface on the graphene materials. The Cu_2O/G material possesses the superior specific capacitance at entire current densities compared with the Cu_2O and graphene electrode materials as shown in Fig. 10(c). A liner growth of specific capacitance in Cu_2O/G nanomaterials is perceived through increasing in current densities. The excellent capacitive property is probably ascribed because of the usage of aqueous electrolyte with higher ionic conductivity as well as the synergistic effect among the graphene and Cu_2O nanomaterials. The graphene on the nanocomposite material hastens the charge transfer over electric dual layer, whereas Cu_2O offers tiny diffusion distance for the electrolyte, high electrochemical active profile for reversible, and fast non-Faradic process. These are consequences in greater surface zone through more active spots and improves the capacitance over supreme capacitive contribution through the robust interface in the electrolyte. The Cu_2O/G electrode achieved

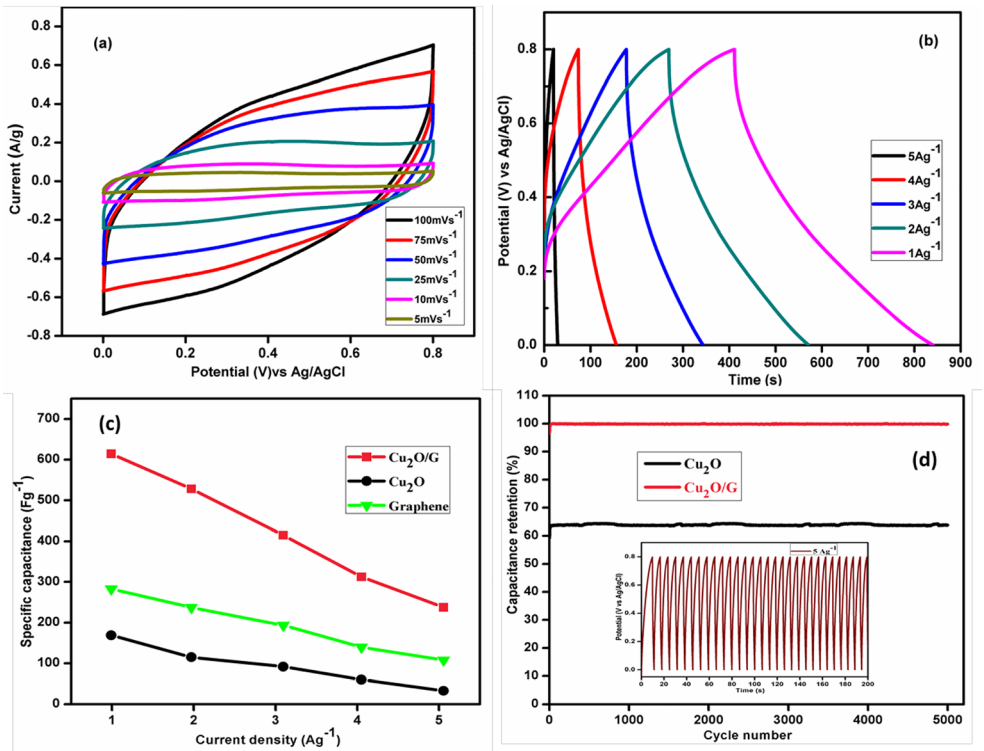

Fig. 10 Cu_2O/graphene composite electrode **a** CV plots of at various sweep rates; **b** CP plots of on several current densities; **c** current densities and specific capacitance; **d** cyclic stability of the nanocomposite electrode

capacitance retention of 99.5% at subsequent 5000 cycles, signifying the outstanding cyclic stability as described in Fig. 10(d). The pure Cu_2O electrode material reveals an unstable retention of 64% because of the perception of electrolyte ions with the regular initiation on the active materials through the beginning in the charge-discharge cyclic procedure. The capacitance withholding in the Cu_2O/G nanocomposite material is greater when compared with Cu_2O electrode material subsequent 5000 rounds because of higher surface region for ion separation and robust affixing Cu_2O nanoparticles over the edges of graphene [15].

3.2.10 Graphene–Mn_3O_4 nanocomposite

The CV graphs of Mn_3O_4 materials are presented in Fig. 11(a) at different sweep rates of 5 to 50 mV/s with the voltage ranging among −0.2 and 0.8 V in 1 M aqueous KOH electrolyte. The computed specific capacitance is 40 F/g on the sweep rate as 5 mV/s. The CV graphs for the Mn_3O_4/rGO (5 wt%) nanocomposite presented in Fig. 11(b) at different sweep rate and the distinctive EDLC behavior was confirmed from the CV curves through the rectangular shape. The calculated specific capacitance for the Mn_3O_4/rGO (145 F/g on 5 mV/s) is greater of pristine Mn_3O_4. The CV graphs of pristine Mn_3O_4 and Mn_3O_4/rGO nanocomposite are presented in Fig. 11(c) for the evaluation. Figure 11(d) offers the specific capacitance deviation because of the sweep rate of pristine Mn_3O_4 and Mn_3O_4/rGO electrodes. The nanocomposite electrode deduces that Mn_3O_4 nanoparticles are introduced inside of the GO sheets and hinder the restacking of rGO nanosheets as well as aggregation of Mn_3O_4 nanoparticles; the electrolyte ions can interact an indubitable way.

From charge–discharge effects, the discharging time was greater for the Mn_3O_4/rGO (5 wt%, 427 F g^{-1}) electrode related to the pristine Mn_3O_4 electrode material (136 F g^{-1}), specifying higher supercapacitance behavior of the material. The schematic of redox response of Mn_3O_4 in the KOH aqueous electrolyte with as-prepared glassy carbon electrode, thus the electrochemical response is quantified by

$$2Mn_3O_4 + 5O_2 + 12KOH = 6K_2MnO_4 + 6H_2O \quad (1)$$

In the charging state, the K^+ ions can electrochemically respond through the Mn3O4 nanoparticle and gives 6K2MnO4 development. Alternatively, K^+ ions are significantly attracted over rGO flacks. Meantime, during the discharge procedure, the K^+ ions are released as of the rGO sheets in advance to the decline of $6K_2MnO_4$ to $2Mn_3O_4$. The greater discharging period of nanocomposite was because of the robust interface of K^+ ions by additional energetic spots over Mn_3O_4 and rGO sheets [16].

3.2.11 Graphene–Yb_2O_3 nanocomposite

The cyclic voltammetry measurements for Yb_2O_3G nanocomposites are recorded through the voltage ranging of −0.1 to 0.4 V in an electrolyte solution of 1 M aqueous H_2SO_4. The

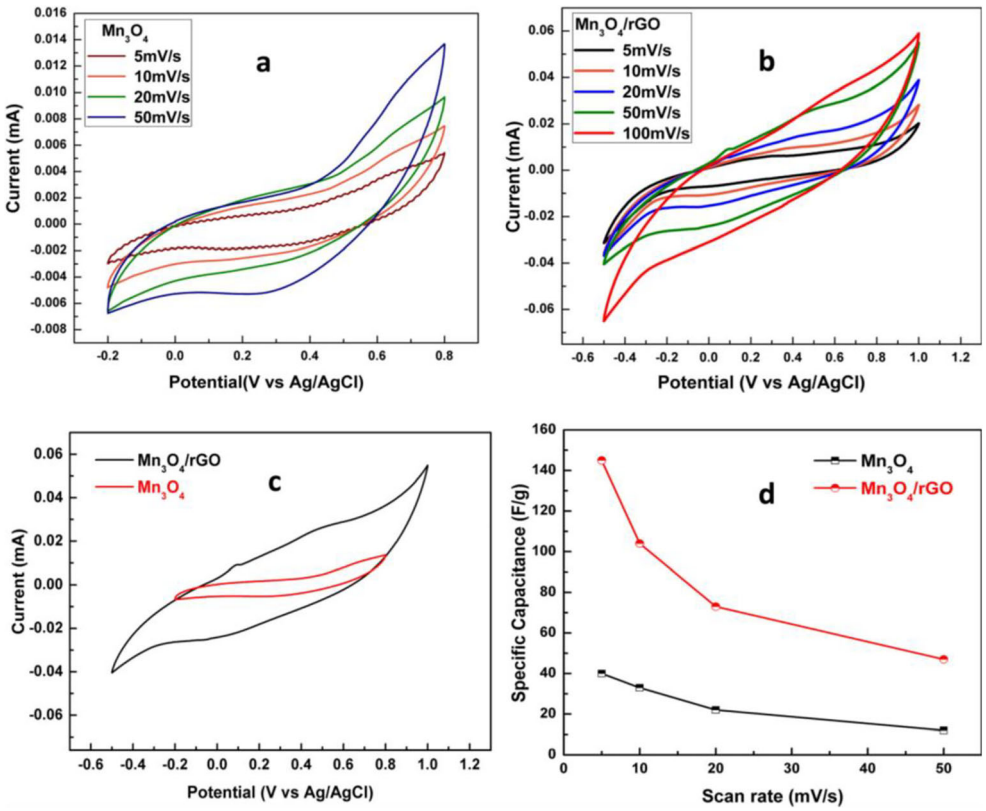

Fig. 11 CV graphs of **a** Mn_3O_4; **b** Mn_3O_4/rGO (5 wt%); **c** evaluation CV graph for Mn_3O_4 and Mn_3O_4/rGO on 50 mV/s; **d** the specific capacitance for Mn_3O_4 and Mn_3O_4/rGO (5 wt%) electrodes

measured voltammogram of pristine Yb_2O_3, Yb_2O_3G1, and Yb_2O_3G5 at numerous sweep rates as 3 to 100 mV/s are revealed in Fig. 12(a–c). The CV measurements for pristine Yb_2O_3 and Yb_2O_3G nanocomposites at the lower scanning rate (3 mV/s) are compared and the voltammograms shown in Fig. 12(d). From the outcomes, it is evident that the rise in

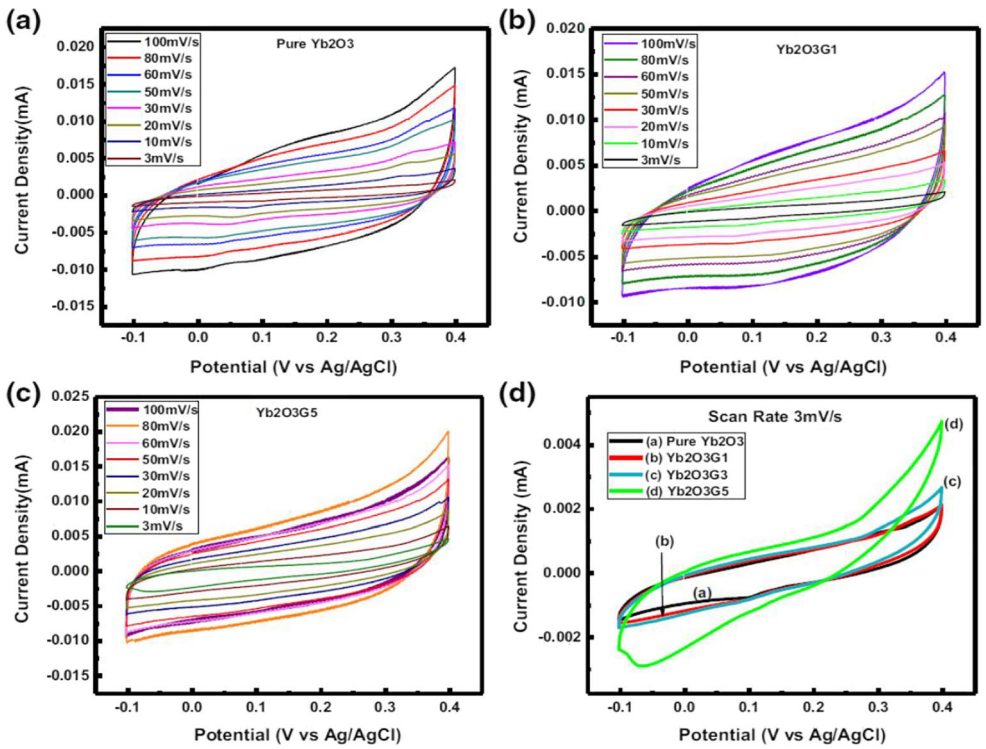

Fig. 12 Cyclic voltammograms for **a** pure Yb_2O_3, **b** Yb_2O_3G1, **c** Yb_2O_3G5 nanocomposites on numerous sweep rates, and **d** evaluation of CV loop for pristine Yb_2O_3, Yb_2O_3G1, Yb_2O_3G3, and Yb_2O_3G5 for the scanning rate on 3 mV/s.

the current density as subjective through the quantity of graphene mixed in the nanocomposites (current study) improves the dual-layer capacitance performance. The higher specific capacitance, 550 F/g for Yb_2O_3G5 nanocomposite sample was perceived on a sweep proportion as 3 mV/s. Instead, the charge–discharge plots for pristine Yb_2O_3, Yb_2O_3G1, Yb_2O_3G3, and Yb_2O_3G5 nanocomposite have been measured on numerous current densities, for further estimation of capacitance behavior [17].

3.2.12 Graphene–$BiYO_3$ nanocomposite

The electrochemical performance of the $BiYO_3$ and $BiYO_3$/RGO nanocomposite materials are estimated through CV analysis. The CV arcs of the materials are measured in the voltage ranging from 0 to 1.0 V vs. Ag/AgCl on sweep rates as 10–50 mV/s are revealed in Fig. 13(a–c). Furthermore, the essential degree of the CV arcs for $BiYO_3$/RGO nanocomposite is seemingly higher compared to $BiYO_3$, specifying that the $BiYO_3$/RGO nanocomposite displays superior specific capacitance compared to $BiYO_3$. The enhancement in the current values of $BiYO_3$/RGO nanocomposite is ascribed in the substitution of RGO and escalates the conductivity and precise surface profile on the pure $BiYO_3$. The clear perception mechanism in the oxidation and reduction process through the CV reaction as comparable to Bi_2O_3, $BiPO_4$, and Bi_2WO_6 nanomaterials.

$$Bi_{(0)} \rightarrow Bi_{(metallic)} \quad (2)$$

$$Bi_{(metallic)} \rightarrow Bi^{+} + e^{-} \quad (3)$$

$$Bi_{(metallic)} \rightarrow Bi^{3+} \quad (4)$$

$$Bi^{3+} + 3\ OH^{-} \rightarrow Bi(OH)_3 \quad (5)$$

$$Bi(OH)_3 \rightarrow\ BiOOH + H_2O \quad (6)$$

$$BiO_2^{2-} + H_2O \rightarrow BiO_2 + 4\ OH^{-} + Bi\ (0) \quad (7)$$

The chrono potentiometric (CP) arcs of $BiYO_3$/RGO nanocomposite are dignified at various current densities of the ranging of 2 to 10 A g^{-1}, and the computed specific capacitances are in consistent with the specific capacitance measured from CV analysis. The extreme capacitance for $BiYO_3$/RGO nanocomposite is 696 F g^{-1} on current density as 2 A g^{-1}; the value is greater as 500 F g^{-1} for $BiYO_3$. The specific capacitance values for the $BiYO_3$/RGO nanocomposite are calculated at increase in current densities as 725, 292, 162, 122, and 100 F g^{-1}, signifying that the specific capacitance decreases by increasing the current densities of the samples [18].

3.2.13 Graphene–Co_3O_4 nanocomposite

The cyclic voltammetry (CV) analysis of Co_3O_4/graphene nanocomposite was studied in the voltage ranging of 0.0 to 0.45 V with various sweep rates with 1 M aqueous KOH electrolyte (revealed in Fig. 14). Figure 14(a) shows the evaluation for CV arcs of the Co_3O_4 and Co_3O_4/graphene nanocomposite electrode materials. The pairs of redox peaks were

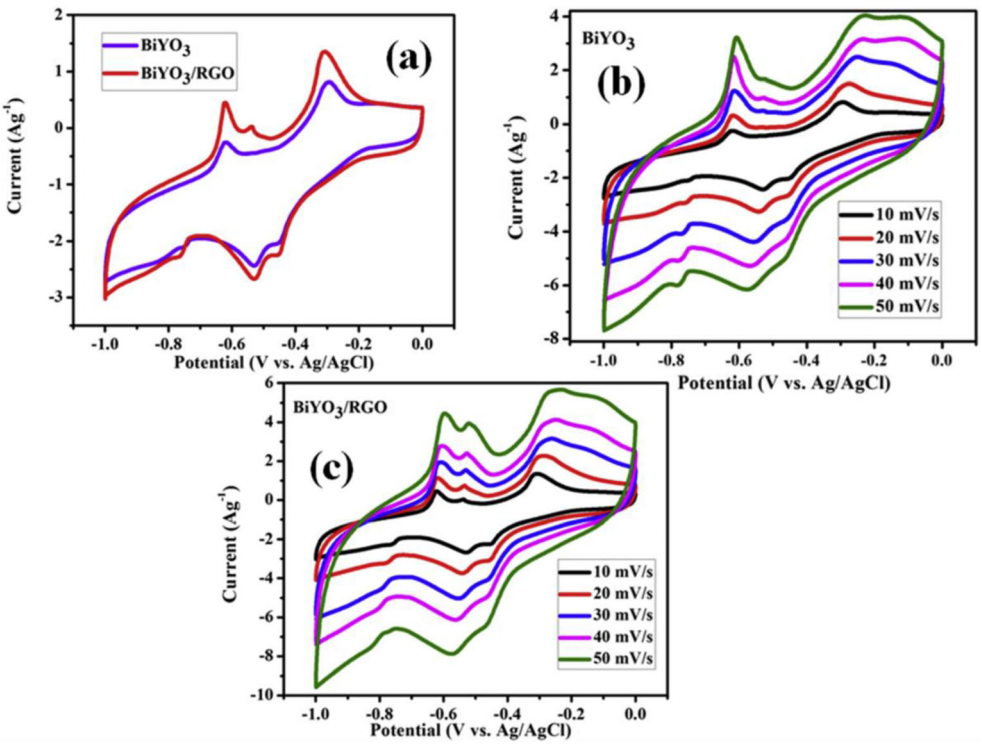

Fig. 13 **a** CV arcs for $BiYO_3$ and $BiYO_3$/RGO nanocomposite on a sweep rate as 10 mV/s; **b**–**c** CV arcs for $BiYO_3$ and $BiYO_3$/RGO nanocomposite on various sweep rates

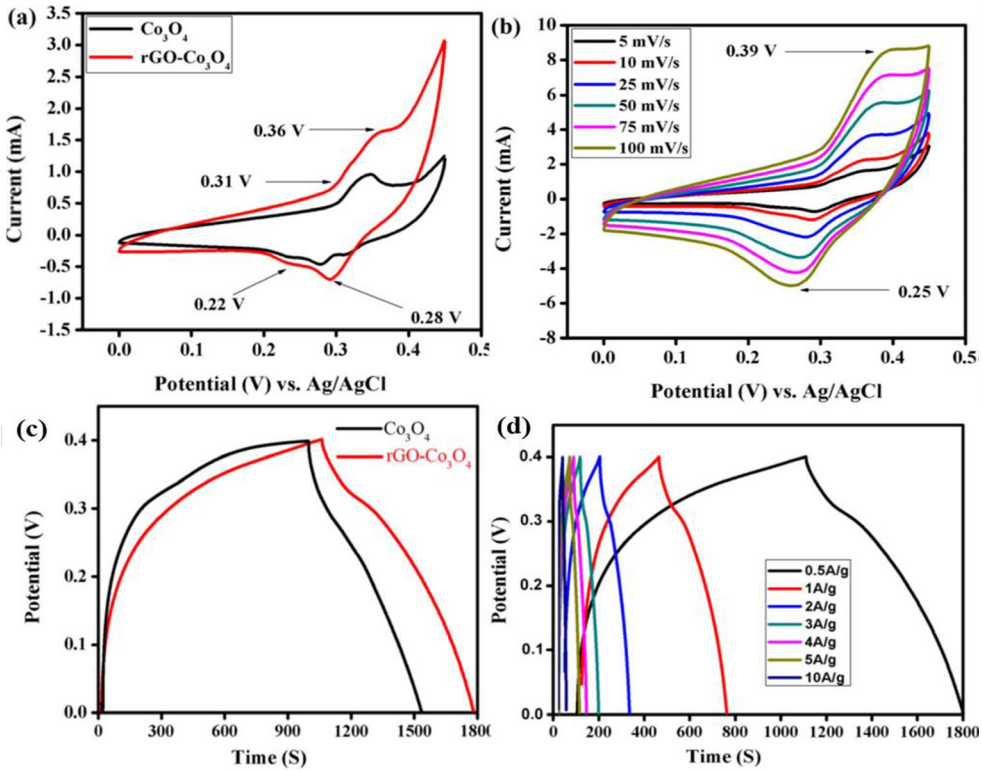

Fig. 14 CV arcs of **a** Co_3O_4 and Co_3O_4/rGO nanocomposite studied on a sweep rate as 5 mV s^{-1} and (b) Co_3O_4/rGO nanocomposite material studied on various sweep rates and CP arcs of **c** Co_3O_4 and the Co_3O_4/graphene nanocomposite measured on current density as 0.5 A g^{-1} and **d** the Co_3O_4/graphene nanocomposite measured on various current densities

observed during anodic and cathodic process on the CV arcs for both electrodes at short sweep rate as 5 mV/s. The Co^{2+}/Co^{3+} and Co^{3+}/Co^{4+} translation processes are confirmed by dual oxidation curves at 0.31 V and 0.36 V. The reverse processes occurs with the reduction curves at 0.22 V and 0.28 V; the peaks are corresponds to dissimilar oxidation states of cobalt. The CV arc of Co_3O_4/rGO nanocomposite electrode possesses an enhanced area because of the embedding of Co_3O_4 onto the graphene sheets which recognized to the Faradaic behavior (pseudocapacitance) from the Co_3O_4. The electrochemical processes can be described as follows:

$$Co_3O_4 + OH^- \longleftrightarrow Co_3O_4\|OH^- + Co_3O_4\text{–}OH \quad (8)$$

$$Co_3O_4 + OH^- + H_2O \longleftrightarrow 3CoOOH + e^- \quad (9)$$

$$CoOOH + OH^- \longleftrightarrow CoO_2 + H_2O + e^- \quad (10)$$

Figure 14(b) reveals the CV arcs of the Co_3O_4/rGO nanocomposite electrode measured at various sweep rates. From the figure, the oxidation peak shifts to optimistic path and the reduction curve shifts to the undesirable direction consequently for scan rate increases from low to high. The area of the CV profile was enhanced for Co_3O_4/rGO nanocomposite because of the embedding of Co_3O_4 over the graphene sheets, which improves the ion distribution and electrical conductivity. The Co_3O_4/rGO nanocomposite material possess greater specific capacitance as 825.51, 592.42, 407.31, 314.29, 268.90, and 241.24 F g^{-1} on the sweep rate as 5, 10, 25, 50, 75, and 100 mV s^{-1}, correspondingly. The specific capacitance for the Co_3O_4/graphene nanocomposite material increases by raising the sweep rate because of the large specific area of graphene, delivers a higher electroactive surface area from graphene, and which permits the OH^- ions interacts efficiently through the active substance in the redox reactions. The calculated specific capacitance of Co_3O_4/graphene nanocomposite is greater than of pristine Co_3O_4, which results enriched electrochemical characteristics of Co_3O_4/graphene nanocomposites.

The CP arcs of the Co_3O_4/graphene composite material are recorded at various current densities. Figure 14(c) displays the CP arcs of Co_3O_4 and the Co_3O_4/graphene nanocomposite are compared. The Co_3O_4/graphene nanocomposite electrode exhibits an extensive charge–discharge time compared to the pure Co_3O_4 electrode because of the improved electrochemical performance and greater specific capacitance. The CP arcs for the nanocomposite measured at various current densities result a symmetric charge–discharge shape shown in Fig. 14(d), which reveals Faradaic (pseudocapacitive) behavior with outstanding electrochemical reversibility. The specific capacitance for the materials is computed through the CP arcs using the standard formulae. A greater specific capacitance, 916.6 F g^{-1} was perceived from Co_3O_4/rGO nanocomposite on a current density as 0.5 A g^{-1} and greater than earlier reported values. The Co_3O_4/rGO

nanocomposite results a maximum Columbic proficiency of 98% rendering to the symmetric charge–discharge arcs. The high-rate performance of the Co_3O_4/rGO nanocomposite are ascribed to two major aspects: (i) the high porosity of the material enriches the electrolyte accessibility, producing extra oxide–electrolyte boundaries for superior redox reactions, and (ii) the nanoarchitecture curtails the electron and ion migrant distances through the oxide, which increases the electrode transfer for enhanced reaction kinetics [19].

3.2.14 Graphene–Mn-MoO_4 nanocomposite

Figure 15 shows the CV arcs of Mn-MoO_4/G nanocomplex, pristine Mn-MoO_4, and GO on various sweep rates in the ranging of 1 to 100 mV s^{-1} by the voltage ranging of −0.8 V to 0.8 V with 1 M of Na_2SO_4 aqueous electrolyte and the competition among the peak current corresponds to the square root on sweep rates. The current density for Mn-MoO_4/G nanocomplex materials are greater as of pristine Mn-MoO_4, illustrating the Mn-MoO_4/G electrode materials possesses higher capacitance and holds the characteristic behavior because of the presence of graphene material. Consequently, the great utility of pseudocapacitive nature of Mn-MoO_4 is accomplished from the Mn-MoO_4/G nanocomplex materials and the consistent CV plots on various sweep rates are revealed in Fig. 15(a). The CV arcs of pristine Mn-MoO_4 (Fig. 15(b)) and Mn-MoO_4/G materials are relatively similar by a pair of wide redox points through the positive and negative scan signifying the pseudocapacitive property. The CV arc of GO is revealed in Fig. 15(c), the arc reproduces the lack in redox peaks by assessed in the sweep ranging from −0.6 to 0.6 V, which possesses the EDLC behavior. Consequently, the tremendous current output from the CV arcs for Mn-MoO_4 and its graphene–grafted nanocomposites directs the fast kinetics in the substantial faradaic redox responses and better proportions of ionic transfer and electronic on the high sweep rate as 100 mV s^{-1}.

Figure 16 shows the chrono potentiometric plots for Mn-MoO_4/G nanocomplex, pristine Mn-MoO_4, GO, and evaluation plot for charge-discharge on smaller current density as 0.1 Ag^{-1}. In the description of chrono potentiometric plots, the discharge period for Mn-MoO_4/G is considerably higher as compared with pristine-Mn-MoO_4 and GO on both small and large current densities, representing the Mn-MoO_4/G nanocomposites confirm a considerably greater capacitance. The responses were in concurrence of the CV outcomes. The Mn-MoO_4/G nanocomplex holds large specific capacitance as 302.08 Fg^{-1} on 0.1 Ag^{-1} correspondingly. The pristine Mn-MoO_4 demonstrates the specific capacitance as 201.81–90.9 on 0.1–1 Ag^{-1} and the GO material has the specific capacitance of 121.39–25.641 Fg^{-1} on 0.1–1 Ag^{-1} correspondingly. As a result, the higher specific capacitance from Mn-MoO4/G nanocomplex specifies a robust synergic influence among graphene and Mn-MoO_4. The capacitance withholding ratio

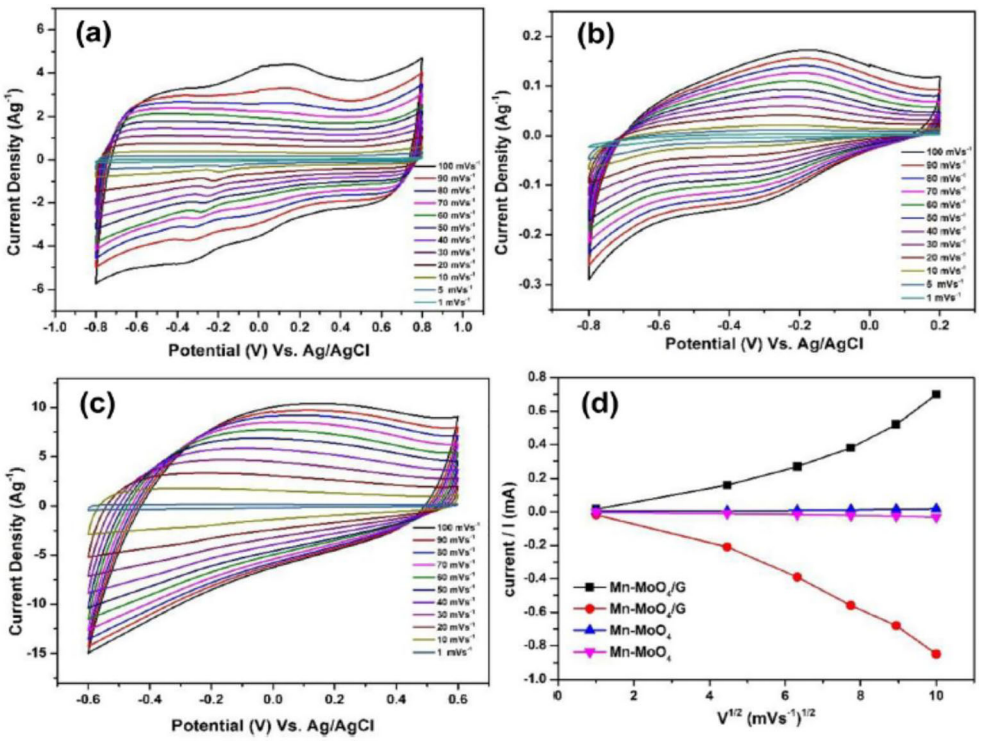

Fig. 15 CV arcs of **a** Mn-MoO_4/G nanocomplex, **b** pristine Mn-MoO_4, **c** GO, and **d** peak current by corresponds to square root on the various sweep rates for pristine Mn-MoO_4 and Mn-MoO_4/G nanocomplex

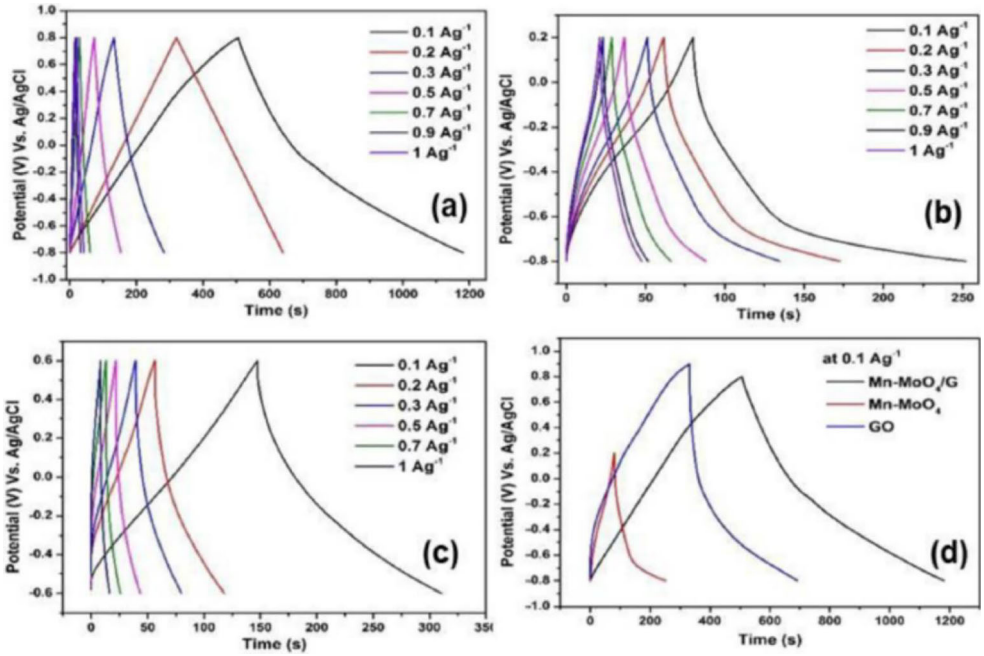

Fig. 16 Chrono potentiometric plots for **a** Mn-MoO_4/G nanocomplex, **b** pristine Mn-MoO_4, **c** GO on the various current densities, **d** evaluation plot for all on 0.1 Ag^{-1}

primarily hinge at a current density through a large retaining as 93.8% on 0.7 Ag^{-1} with 41.9 Wh kg^{-1} as energy density and 208 W kg^{-1} as power density and it's greater related to pristine Mn-MoO_4. The enhanced electrochemical process are because of the rise in electrode conductivity of the existence in graphene network, the improved active interfacing profile among Mn-MoO_4, electrolyte, and the interaction region among graphene and Mn-MoO_4 [20].

3.2.15 Graphene–a-MoO_3 nanocomposite

CV plot for a-MoO_3 and a-MoO_3/G nanocomplex are revealed in Fig. 17 with the potential window as 0.0 to 1.0 V

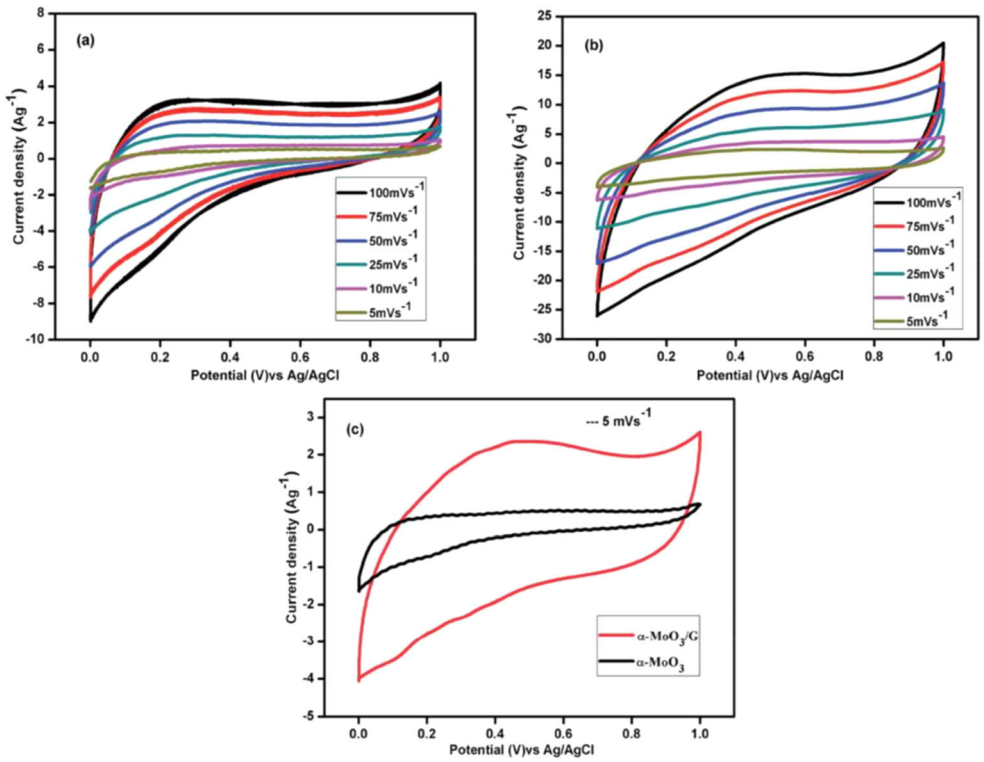

Fig. 17 CV plots for **a** a-MoO_3, **b** a-MoO_3/G nanocomposite electrode on various sweep proportions, **c** evaluation CV for a-MoO_3 and a-MoO_3/G nanocomposite on a sweep rate as 5 mV s^{-1}

in tri-electrode system through 1 M aqueous H_2SO_4 solution. The CV plots of the a-MoO_3 material was measured on numerous sweep rates as 5, 10, 25, 50, 75, and 100 mV s^{-1} in an ambient temperature as revealed in Fig. 17(a). The CV sweeps on 100 mV s^{-1} through minor alteration in rectangular profile related to 5 mV s^{-1}, which is because of the kinetics on the ion transportation process at the electrode and the ion adsorption/desorption in the electrode/electrolyte boundary are lesser. The Fig. 17(b) shows the CV plots of a-MoO_3/G composite revealing almost rectangular profile without the redox plot, suggesting a superior capacitive behavior, signifying the quick charging/discharging routes. The CV plots of a-MoO3 and a-MoO_3/G nanocomposites on a sweep proportion as 5 mV s^{-1} are related in Fig. 17(c). The integral region in the CV plots of a-MoO_3/G nanocomposite was greater than of pristine a-MoO_3 materials. The advanced electrical conductivity for a-MoO_3/G nanocomposites effectually raises the conducting paths of the ions and decreases the EDL capacitance, hence growing the active region in CV of a-MoO_3 composite material. In addition, a-MoO_3 composite shows huge contact region of the electrolyte ions and raises the capacitance through decreasing the distortion.

Figure 18(a) describes the charge–discharge plot for a-MoO_3 on various current densities typically ranging of 1 to 5 A g^{-1} with the voltage range 0–1.0 V. The CP plots signify close symmetrical and triangular profile without any change in interior resistance (IR). The CP plots for pristine a-MoO_3/G revealed in Fig. 18(b) are alike and closely symmetrical, signifying a greater reversibility because of EDLC and pseudocapacitance behavior of the materials designed for the quick charge–discharge method. The evaluation of CP plots for both pristine and composite on a constant current density as 1 A g^{-1} are revealed in Fig. 18(c). The calculated specific capacitance for a-MoO_3/G nanocomposite was 483, 354, 268, 190, 151 F g^{-1}, and a-MoO_3 materials was 142, 89, 56, 23, 14 F g^{-1} correspondingly on various current densities. The preservation of the composite material deliberated through the CP study of 5000 cycles, the capacitance of the nanocomposite rises by increasing cycles and accomplished 100% cyclic retention up to 5000 cycles [21].

3.2.16 Graphene–Nb_2O_5 nanocomposite

Figure 19(a) shows the characteristic cyclic voltammogram (CV) arcs for the Nb_2O_5 electrode material at the potential ranging of −0.45 to 1.0 V on several sweep rates with 1 M aqueous H_2SO_4 electrolyte. The CV arcs for Nb_2O_5 reveal oxidation and reduction curves at the sweep rate as 5 to 100 mV s^{-1}, obviously due to the features of Faradic behavior. The CV arcs are shown Fig. 19(b) reveal a quasi-rectangular profile lacking oxidation and reduction curves signifying the greater constancy for Nb_2O_5/G nanocomposite electrodes in a broader voltage range also which discloses exceptional reversibility and earlier surface reaction. The results authorize that the Nb_2O_5/G nanocomposite material possess outstanding capacitance property and short contact resistance, delivered from the large surface profile. Figure 19(c) displays the evaluation CV arcs for pristine Nb_2O_5 and Nb_2O_5/G nanocomposites

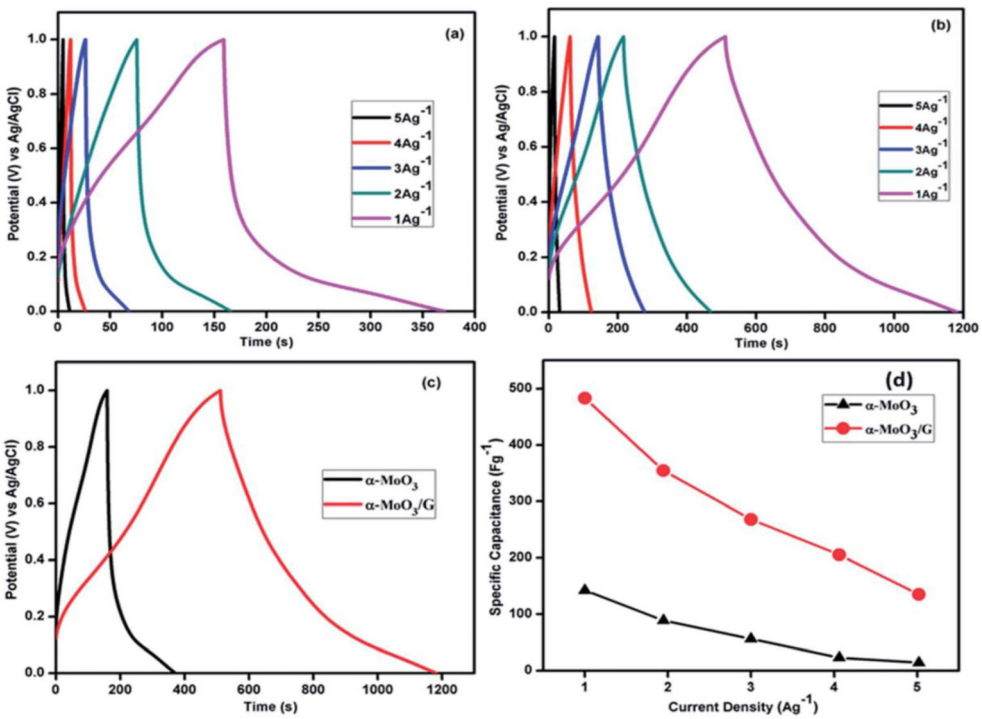

Fig. 18 CP plots for **a** a-MoO_3; **b** a-MoO_3/G nanocomposite material on various current densities; **c** evaluation CP plots; **d** specific capacitance for a-MoO_3 and a-MoO_3/G nanocomposite on various current densities

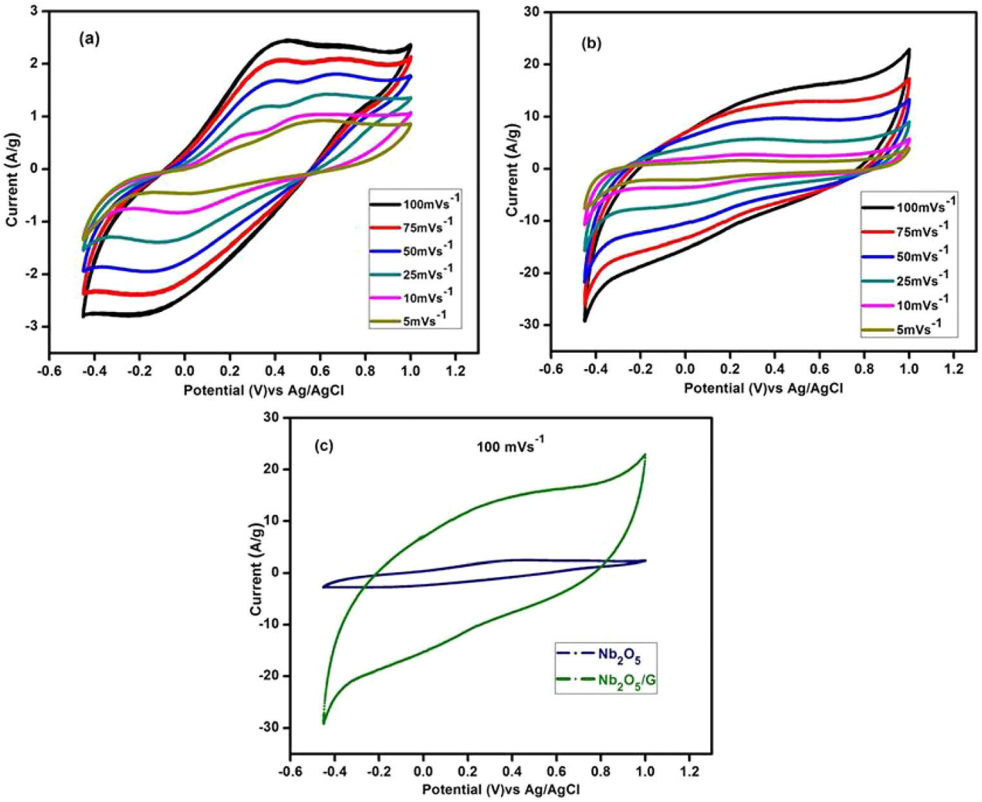

Fig. 19 Cyclic voltamogram arcs of **a** Nb_2O_5, **b** Nb_2O_5/G nanocomposite on numerous sweep rates, and **c** evaluation CV arcs for Nb_2O_5, and Nb_2O_5/G on a sweep rate as 100 mVs^{-1}

materials on a sweep rate as 100 mV s^{-1}. The specific capacitance (C_s) for pristine Nb_2O_5 and Nb_2O_5/G nanocomposites are calculated using CP arcs. The specific capacitance calculated are 633, 271, 445, 314.8, 238.1, 168.9 Fg^{-1} for Nb_2O_5/G nanocomposite and 221, 168.5, 82.1, 34.5, 19 Fg^{-1} for pristine Nb_2O_5 materials, correspondingly on numerous current densities. The response on both materials reduced by raising the current density ranging of 1 to 5 Ag^{-1}. Additionally highly distributed Nb_2O_5 nanoparticles prevent the restacking in G sheets to support greater surface region for the storage. The capacitance retention of the Nb_2O_5/G nanocomposite preserve a stability as 99.3% at subsequent 5000 rounds without decline, signifying the outstanding electrochemical constancy in the material, which is greater than pristine Nb_2O_5 electrode material. The Nb_2O_5/G nanocomposite material maintains the Coulombic efficiency as 99.5% for the consequent in symmetrical charge-discharge arcs [22].

3.2.17 Graphene–V_2O_5 nanocomposite fibers

The capacitance performance witnessed for graphene oxide/V_2O_5 fibers heat treated at 550 °C and studied by changing the sweep rate in three-electrode cell system of the cyclic voltammetry. Figure 20 displays the characteristic CV graphs

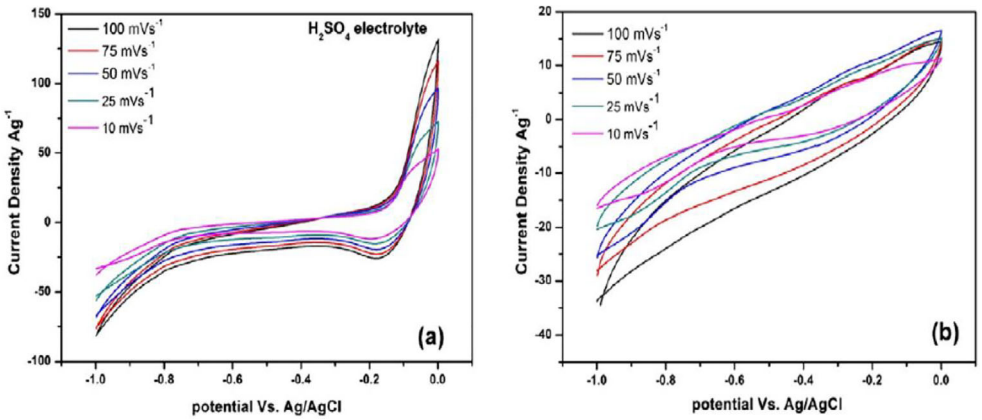

Fig. 20 **a** and **b** CV graphs of graphene oxide/V_2O_5 nanofibers on various electrolytes (aqueous KOH and H_2SO_4)

recorded for VO, GO, and GVO fibers on the sweep rate as 10 to 100 mV s^{-1} with 2 M aqueous KOH electrolyte. The specific capacitance for VO, GO, and GVO is calculated through the CV graphs and laden mass for VO, GO, and GVO is roughly 2 mg. The calculated specific capacitance in GO are 306.9, 348.5, 409.2, 454, and 540.4 Fg^{-1}, for VO are 109.5, 120.5, 138.65, 168.51, and 252.7 Fg^{-1} and for GVO are 111.01, 111.38, 149.74, 255.26, and 453.824 Fg^{-1} at the sweep proportions as 100, 75, 50, 25, and 10 mV s^{-1} separately [23].

3.2.18 Graphene–WO_3 and graphene–CuO/ZnO/Ag nanocomposite

The tungsten oxide (WO_3) and reduced graphene oxide (rGO) nanocomposites are used as ozone molecule sensing at small ppm range in ambient temperature. For ozone sensing, the pure WO_3 and rGO/WO_3 nanocomposite materials are used; these materials are experimentally synthesized by using hydrothermal method. Among the two materials, the rGO/WO_3 nanocomposite material possesses higher sensing response even at substandard environment [24].

The phase change behavior of graphene and metal oxide composites can be used for phase change materials (PCMs) as energy storage of thermal heat. The PCMs composites are synthesized through the caprylic acid precursor constituent while, Ag, CuO, ZnO, and GO are supportive constituents. The caprylic acid thermal conductivity enriches through 0.5 wt% as Ag, CuO, ZnO, and GO NPs distinctly, is expected results of 36%, 43%, 52%, and 87%, separately while likened with caprylic acid only. The outcomes attained on the investigation confirmed the melting and freezing periods for the PCM composites by GO are fewer, compared with the remaining. Hence, GO created PCM composites are used as a right constituent for short temperature thermal energy storing application [25].

3.3 Electrochemical property of threefold rGO nanocomposites

3.3.1 Graphene-CNT/CeO_2 threefold nanocomposite

Figure 21 illustrates the CV graphs for twofold CNT/CeO_2 and threefold RGO/CNT/CeO_2 nanocomposites in the voltage ranging of −1.0 to 0.0 V studied on numerous sweep rates (5–100 mV s^{-1}). The CV graphs for CNT/CeO_2 (Fig. 21(a)) displays a rectangular profile of all sweep rates viewing the electrical dual-layer capacitor characteristics. The charge and discharge take place on the quasi persistent rate through the whole volumetric series. Substantial improvement in the electrochemical enactment might be attained from the threefold RGO/CNT/CeO_2 nanocomposites (Fig. 21(b)). The whole region on the CV graph for RGO/CNT/CeO_2 considerably extended, which suggesting as an improved capacitance related to

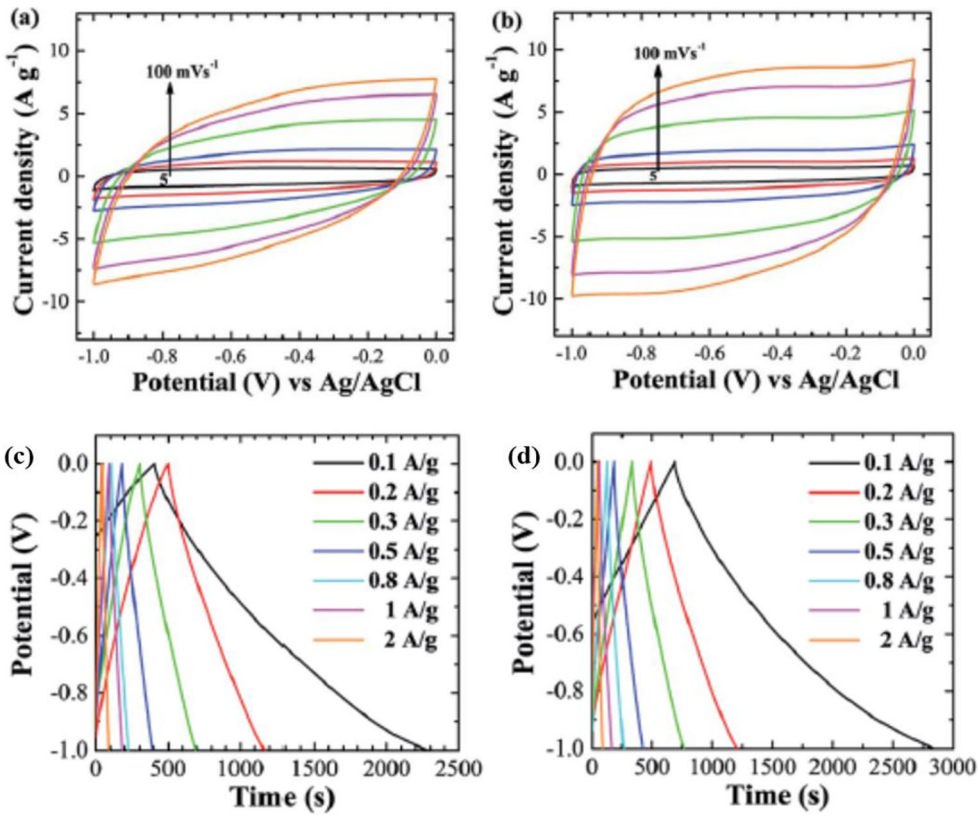

Fig. 21 Electrochemical characteristics for twofold CNT/CeO_2 and threefold RGO/CNT/CeO_2 nanocomposite: CV graphs for CNT/CeO_2 **a** consistent CV graphs for RGO/CNT/CeO_2 nanocomposites and **b** on various sweep rates as 5, 10, 20, 50, 80, and 100 mV s^{-1} with 1 M Na_2SO_4 aqueous solution and chronopotentiometry (CP) graphs; **c** for RGO/CNT/CeO_2 electrode material on various current densities; **d** for all electrode materials on a static current density as 0.1 A g^{-1}

CNT/CeO_2. The outstanding capacitance characteristics for the threefold nanocomposite are ascribed as the identical sharing of CeO_2 nanomaterials over the CNTs with superior conductivity on RGO.

Galvanostatic charge–discharge (C-D) graphs for CeO_2, CNT/CeO_2, and $RGO/CNT/CeO_2$ electrode materials formed over the glassy carbon electrode are studied on various current densities (0.1 to 2.0 A g^{-1}) in an voltage ranging of −1.0 to 0 V (Fig. 21(c–d)). The $RGO/CNT/CeO_2$ electrode material obviously possesses extended discharge period related to CeO_2 and CNT/CeO_2 electrodes. On a current density as 0.1 A g^{-1}, the specific capacitance calculated for CeO_2, CNT/CeO_2, and $RGO/CNT/CeO_2$ nanocomposites are 37, 188, and 215 F g^{-1}, correspondingly. This proves the dimensional combined nanocomposite through 0D CeO_2, 1D CNT, and 2D RGO nanomaterials, the threefold $RGO/CNT/CeO_2$ nanocomposite remains the finest from the specific constituents or CeO_2 nanocomposites by CNTs because the CNTs performs an inserts towards inhibition of restacking in RGO, which prevents the agglomeration of CeO_2 nanomaterials. The durability analysis of CeO_2, CNT/CeO_2, and $RGO/CNT/CeO_2$ are studied with CP graphs of numerous phases on 1 A g^{-1} and the threefold nanocomposite electrode reveals outstanding cycling constancy, retentive to 85% of the original capacity at subsequent 1000 cycles [26].

3.3.2 Graphene-CNT/NiO threefold nanocomposite

Electrochemical characteristics for NiO nanomaterials and threefold RGO/CNT/NiO nanocomposite are recorded through CV and galvanostatic charge–discharge (C-D) with 6 M KOH aqueous solution on 25 °C using Ag/AgCl standard potential ranging of −0.1 to 0.4 V on various sweep rates (such as 5, 10 20, 50, 80, 100 mV s^{-1}) shown in Fig. 22. Each CV plot displays a redox pair and the current density rises through sweep rate. The redox pairs agree with the faradaic response of NiO specified in Eq. (11).

$$NiO + OH^- \longleftrightarrow NiOOH + e^- \quad (11)$$

The CV plots for threefold RGO/CNT/NiO nanocomposite is prolonged and related with the NiO nanoparticles in Fig. 22(b) and supplemented by strong redox pairs to each CV plot representing the improved capacitance of threefold nanocomposite and is supposed to the synergic outcome initiated over the addition of NiO on CNT/RGO carbon nanocomposite. In addition, the investigation of the electrochemical characteristics for the NiO and threefold RGO/CNT/NiO nanocomposite electrodes are done by choronopotentiometry analysis with the voltage ranging of −0.1 to 0.4 V (vs Ag/AgCl) on various current densities (such as 1, 2, 3, 4, and 5 Ag^{-1}). The threefold electrode RGO/CNT/NiO nanocomposite revealed a significantly extensive discharge period compared the NiO electrode because of higher dimensions of redox process initiated in the identical arrangement with better number on energetic positions for the threefold nanocomposite electrode. The calculated specific capacitance for the threefold RGO/CNT/NiO electrode material are 367, 166, 152, 142, and 134 F g^{-1} in current densities as 1, 2, 3, 4, and 5 A g^{-1}, correspondingly and are greater compared with NiO nanomaterials (such as 172, 164, 144, 128, and 110 F g^{-1} in 1, 2, 3, 4, and 5 A g^{-1}, separately) [27].

3.3.3 Graphene-Mn_2O_3:Co_3O_4 threefold nanocomposite

CV arcs studied in the voltage range of −0.5 to 0 V (on Mn_2O_3), 0 to 0.6 V (on Co_3O_4), −0.5 to +0.5 V (on MC), and − 0.5 to +0.5 V (on GMC) with 2 M KOH aqueous electrolyte are revealed in Fig. 23. The Co_3O_4 revealed large integral region related to Mn_2O_3, presenting improved pseudocapacitance behavior of faradaic redox response as of the Co^{2+} and Co^{3+} ions. The calculated specific capacitance (Cs) for the GMC nanocomposite electrode (210 F g^{-1} in 5 mV s^{-1}) is far superior to RGO. The capacitance withholding is assessed around 27% on higher sweep rate as 100 mV s^{-1}. The Cs for MC is 186 F g^{-1} in 5 mV s^{-1} through capacitance withholding as around 24% in 100 mV s^{-1}. Besides, the

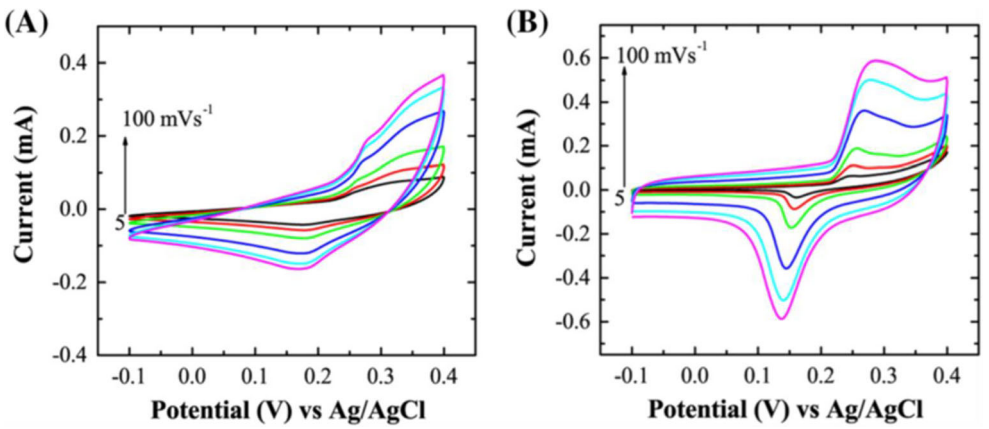

Fig. 22 Electrochemical characteristics for NiO and RGO/CNT/NiO threefold nanocomposite: CV plots for NiO, **a** the consistent CV plots for RGO/CNT/NiO nanocomposite and **b** on various sweep rates as 5, 10, 20, 50, 80, 100 mVs^{-1} with 6 M KOH aqueous solution

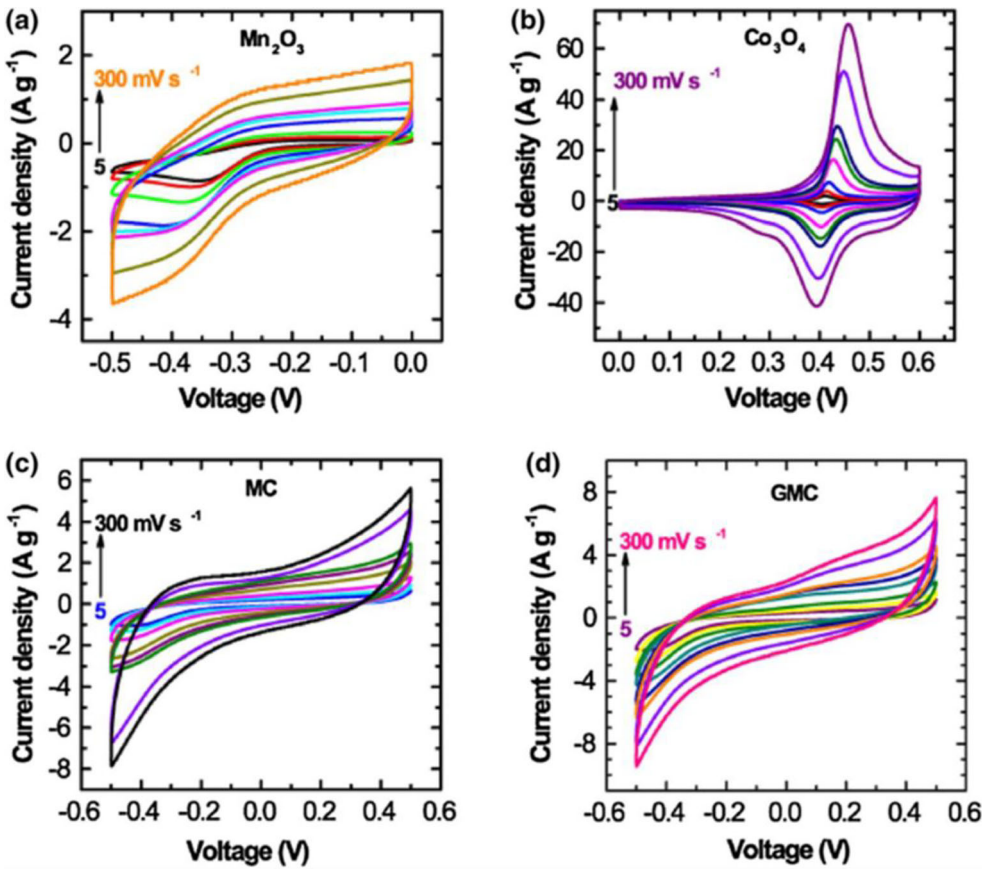

Fig. 23 CV arcs of **a** Mn_2O_3, **b** Co_3O_4, **c** Mn_2O_3:Co_3O_4 (MC), and **d** graphene-Mn_2O_3:Co_3O_4 (GMC) on various sweep rates (such as 5, 10, 20, 50, 80, 100, 200, and 300 mV s^{-1})

electrochemical characteristic for MC and GMC was analyzed through chronopotentiometry in addition to the CV, the galvanostatic charge/discharge (CD) arcs on numerous current densities (such as 2, 3, 4, 5, and 10 A g^{-1}). The computed specific capacitance through CD arc demonstrates the GMC characteristics marginally superior to the MC with a specific capacitance as 184 F g^{-1} in 2 A g^{-1}. Around 12% capacitance withholding is perceived on a greater current density as 10 A g^{-1}. GMC electrode materials revealed outstanding cyclic stability retaining around 87% capacitance withholding at subsequent 1000 cycles signifying that the potential usage of GMC nanocomposite material for supercapacitor application [26].

3.3.4 Graphene-In_2O_3/CNT threefold nanocomposite

Electrochemical analysis for a threefold nanocomposite with Indium oxide (In_2O_3) mesoporous nanocubic crystals (size ~50 nm) implanted carbon nanotubes (CNT) in addition to reduced graphene oxide (RGO) are synthesized using hydrothermal technique. Electrochemical measurements of In_2O_3 mesoporous crystals, twofold In_2O_3/RGO and threefold In_2O_3/CNT/RGO nanocomposite materials are deliberated using cyclic voltammetry with a 2 M KOH aqueous electrolyte. Figure 24(a) shows the comparison CV plots for In_2O_3, In_2O_3/RGO, and In_2O_3/CNT/RGO measured on 5 mV s^{-1} which indicates the fusion supercapacitive performance for the nanocomposite materials. The Cs for In_2O_3/CNT/RGO nanocomposite materials 1237 F g^{-1} is far greater as Cs for In_2O_3 (193 F g^{-1}) and In_2O_3/RGO (630 F g^{-1}). The CV plots with different sweep rate of samples are shown in Fig. 24(b) (In_2O_3), Fig. 24(c) (In_2O_3/CNT/RGO). The Cs values acquired on numerous sweep rates as 5, 10, 20, 50, 80, 100, and 200 mV s^{-1} for In_2O_3 materials are such as 193, 156, 94, 91, 75, 72, and 55 F g^{-1} (28.6% retention), for In_2O_3/RGO materials are such as 630, 557, 486, 446, 421, 408, and 376 F g^{-1} (59.1% retention) and for the In_2O_3/CNT/RGO materials are such as 1273, 1201, 1128,1050, 1014, 997, and 954 F g^{-1} (74.9% retention), correspondingly as revealed in Fig. 24(d).

Electrochemical analysis of the materials was also measured by chronopotentiometry. Figure 25 displays the galvanostatic charge/discharge (CD) plots for In_2O_3, In_2O_3/RGO, and In_2O_3/CNT/RGO nanocomposite materials on a current density as 1 A g^{-1}. The Cs of the samples are 155 F g^{-1} (In_2O_3), 694 F g^{-1} (In_2O_3/RGO) as well as 948 F g^{-1} (In_2O_3/CNT/RGO). The outcomes attained during charge/discharge analysis are in-contract to the CV data of the threefold In_2O_3/CNT/RGO nanocomposite, which displays the more energy storage

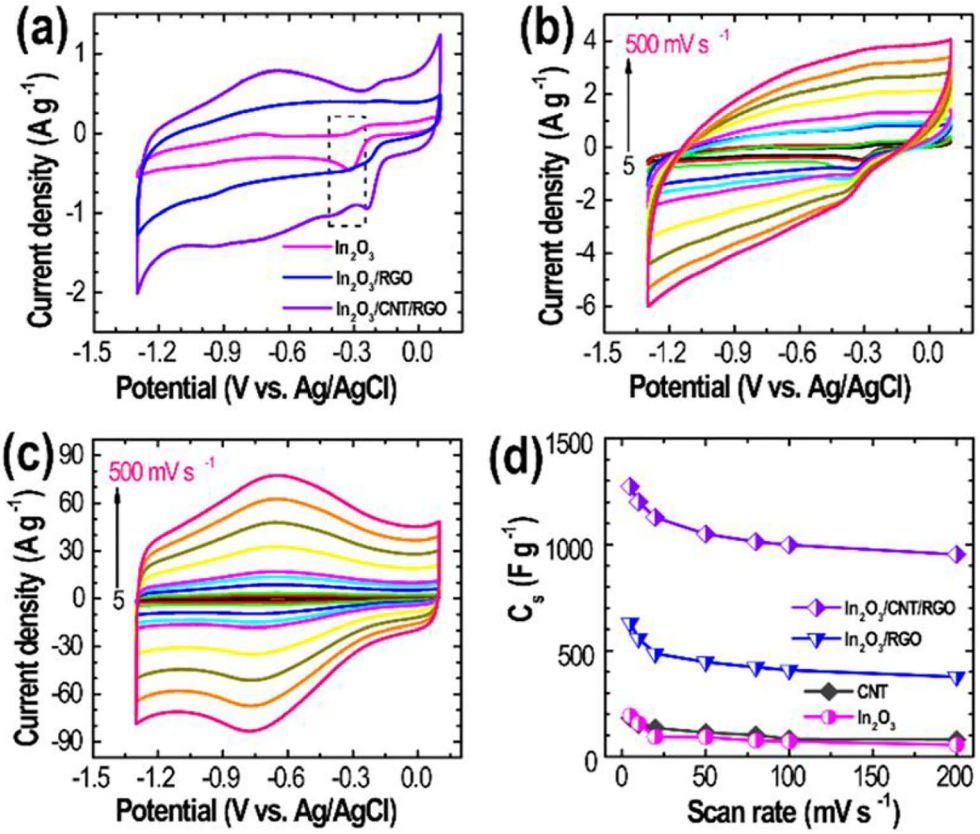

Fig. 24 **a** CV plots for In_2O_3, In_2O_3/RGO, and In_2O_3/CNT/RGO materials on a sweep rate as 5 mV s^{-1}, **b** CV plots for In_2O_3 materials on various sweep rates (5–500 mV s^{-1}), **c** consistent CV plots for In_2O_3/CNT/RGO nanocomposite material on various sweep rates (5–500 mV s^{-1}), **d** computed specific capacitances for In_2O_3, CNT, In_2O_3/RGO, and In_2O_3/CNT/RGO materials

characteristics as related with the pristine In_2O_3 and twofold nanocomposites. Cyclic constancy of the materials are verified as 5000 charge/discharge series in 20 A g^{-1}. From CV and CD results, the ternary nanocomposite material comprising morphologically combined cube-shaped 3D mesoporous crystals

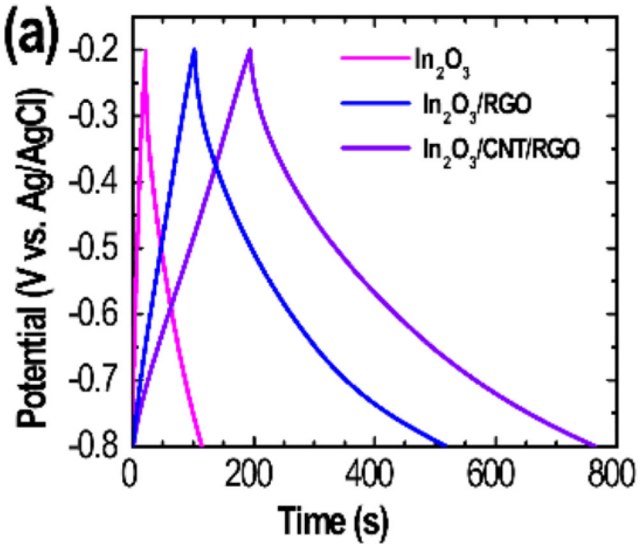

Fig. 25 Galvanostatic charge/discharge (CD) plots for In_2O_3, In_2O_3/RGO, and In_2O_3/CNT/RGO electrode materials on a current density as 1 A g^{-1}

In_2O_3, 2D RGO, and 1D CNT displays an improved supercapacitive process through greater specific capacitance when related with large surface region of nanoporous carbon constituents. The probability of the improved supercapacitive performance is because of the good conductivity on the indium oxide composed through the mesoporous arrangement wherever electrolyte ions are interacted outside/inside of the porous arrangement [29].

3.4 rGO papers for energy application

The investigational outcomes propose that the flexible rGO papers are utilized as a bimorphic electronic actuators at different applied potentials [32]. The nitrogen doped rGO paper–based supercapacitor possesses the specific capacitance as 397 F g^{-1}, larger compared through the conventional liquid electrolyte systems [33]. The power transformation efficiency of 8.96% was attained for the hybrid FTO/TiO_2/$CH_3NH_3PbI_3$/B-rGO/FTO solar cell arrangement in an active region as 1 cm^2 [34]. The metal oxide and graphene based nanocomposite flexible paper–like materials are used for ammonia gas sensing. The metal and graphene nanocomposites are pure rGO, CeO_2-rGO, and SnO_2-rGO nanocomposites and impedance analyzer was used to measure the sensing property under various humidity and concentration. Among the samples, the CeO_2-rGO nanocomposite paper results high compassion as

51.70 ± 1.2%. The metal oxide–based reduced graphene oxide can be applied as a real time sensor application [35].

4 Conclusion

The study on graphene and metal oxide–grafted graphene nanocomposites as energy applications are reviewed. The electrochemical characteristics of graphene-metal oxide nanocomposites are significantly enhanced because of the pseudocapacitance of the metal oxides and the influence of the double-layer capacitance in graphene sheet. The synergistic effect of 2D graphene layers and 3D metal oxide nanostructure provide strong cyclic stability for the electrode suitable for sustainable usage. The results suggest that the graphene metal oxide–based nanocomposites are commonly used for supercapacitors application for energy storage applications.

Declarations

Conflict of interest The authors declare that they have no conflict of interest.

References

1. K. Satheesh, R. Jayavel, Synthesis and electrochemical properties of reduced graphene oxide via chemical reduction using thiourea as a reducing agent. Mater. Lett. **113**, 5–8 (2013)
2. V. Thirumal, A. Pandurangan, R. Jayavel, K.S. Venkatesh, N.S. Palani, R. Ragavan, R. Ilangovan, Single pot electrochemical synthesis of functionalized and phosphorus doped graphene nanosheets for supercapacitor applications. J. Mater. Sci. Mater. Electron. **26**, 6319–6328 (2015)
3. V. Thirumal, A. Pandurangan, R. Jayavel, R. Ilangovan, Synthesis and characterization of boron doped graphene nanosheets for supercapacitor applications. Synth. Met. **220**, 524–532 (2016)
4. S. Dorothy, T. Lavanya, K. Punithamurthy, R. Jayavel, K. Satheesh, Optical characterization and electrochemical properties of Cd(1− x)Cu(x)S/rGO Composites synthesized through reflux method. J. Nanosci. Nanotechnol. **16**, 9716–9721 (2016)
5. T. Saravanan, M. Shanmugam, P. Anandan, M. Azhagurajan, K. Pazhanivel, M. Arivanandhan, Y. Hayakawa, R. Jayavel, Facile synthesis of graphene-CeO_2 nanocomposites with enhanced electrochemical properties for supercapacitors. Dalton Trans. **44**, 9901–9908 (2015)
6. M. Murugan, R.M. Kumar, A. Alsalme, A. Alghamdi, R. Jayavel, Facile hydrothermal preparation of niobium pentaoxide decorated reduced graphene oxide nanocomposites for supercapacitor applications. Chem. Phys. Lett. **650**, 35–40 (2016)
7. V. Rajeswari, R. Jayavel, A. Clara Dhanemozhi, Synthesis and characterization of graphene-zinc oxide nanocomposite electrode material for supercapacitor applications. Mater. Today Proc. **4**(2), 645–652 (2017). https://doi.org/10.1016/j.matpr.2017.01.068
8. R. Thangappan, S. Kalaiselvam, A. Elayaperumal, R. Jayavel, M. Arivanandhan, R. Karthikeyan, Y. Hayakawa, Graphene decorated with MoS2 nanosheets: a synergetic energy storage composite electrode for supercapacitor applications. Dalton Trans. **45**, 2637–2646 (2016)
9. P. Nagaraju, A. Alsalme, A. Alswieleh, R. Jayavel, Facile in-situ microwave irradiation synthesis of TiO2/graphene nanocomposite for high-performance supercapacitor applications. J. Electroanal. Chem. **808**, 90–100 (2018)
10. P. Nagaraju, A. Alsalme, A.M. Alkathiri, R. Jayavel, Rapid synthesis of WO3/graphene nanocomposite via in-situ microwave method with improved electrochemical properties. J. Phys. Chem. Solids **120**, 250–260 (2018)
11. N.A. Kalam, C. Sengottaiyan, R. Jayavel, K. Ariga, R.G. Shrestha, T. Subramani, S. Sankar, L.K. Shrestha, Vanadium sulfide/reduced graphene oxide composite with enhanced supercapacitance performance. J. Taiwan Inst. Chem. Eng. **92**, 72–79 (2018)
12. R. Thangappan, M. Arivanandhan, R. Dhinesh Kumar, R. Jayavel, Facile synthesis of RuO2 nanoparticles anchored on graphene nanosheets for high performance composite electrode for supercapacitor applications. J. Phys. Chem. Solids **121**, 339–349 (2018)
13. T. Saravanan, P. Anandan, M. Shanmugam, T. Jayakumari, M. Arivanandhan, M. Azhagurajan, Y. Hayakawa, R. Jayavel, Impact of graphene on the enhancement of electrochemical and photocatalytic performance of Gd2O3 - graphene nanocomposites. Solid State Sci. **83**, 171–180 (2018)
14. C. Sengottaiyan, N.A. Kalam, R. Jayavel, R.G. Shrestha, T. Subramani, S. Sankar, J.P. Hill, L.K. Shrestha, K. Ariga, BiVO4/RGO hybrid nanostructure for high performance electrochemical supercapacitor. J. Solid State Chem. **269**, 409–418 (2019)
15. P. Nagaraju, R. Vasudevan, M. Arivanandhan, A. Alsalme, R. Jayavel, High-performance electrochemical capacitor based on cuprous oxide/graphene nanocomposite electrode material synthesized by microwave irradiation method. Emergent Mater. **2**, 495–504 (2019)
16. M.M. Ismail, S. Hemaanandhan, D. Mani, M. Arivanandhan, G. Anbalagan, R. Jayavel, Facile preparation of Mn3O4/rGO hybrid nanocomposite by sol gel in situ reduction method with enhanced energy storage performance for supercapacitor applications. J. Sol-Gel Sci. Technol. **93**, 703–713 (2019)
17. T. Saravanan, P. Anandan, M. Shanmugam, M. Azhagurajan, M.M. Ismail, M. Arivanandhan, Y. Hayakawa, R. Jayavel, Facile synthesis of Yb2OS graphene nanocomposites for enhanced energy and environmental applications. Polym. Bull. **77**, 3891–3906 (2019)
18. R. Selvarajan, S. Vadivel, M. Arivanandhan, R. Jayavel, Facile synthesis of pervoskite type BiYO3 embedded reduced graphene oxide (RGO) composite for supercapacitor applications. Ceram. Int. **46**, 3471–3478 (2020)
19. V. Venkatachalam, R. Jayavel, 1D/2D Co3O4/Graphene composite electrodes for high-performance supercapacitor applications. J. Electron. Mater. **49**, 3174–3181 (2020)
20. R. Thangappan, R. Dhinesh Kumar, R. Jayavel, Synthesis, structural and electrochemical properties of Mn-MoO4/graphene nanocomposite electrode material with improved performance for supercapacitor application. J. Energy Storage **27**, 101069 (2020)
21. P. Nagaraju, M. Arivanandhan, A. Alsalme, A. Alghamdi, R. Jayavel, Enhanced electrochemical performance of α-MoO3/graphene nanocomposites prepared by an in situ microwave irradiation technique for energy storage applications. RSC Adv. **10**, 22836–22847 (2020)
22. P. Nagaraju, R. Vasudevan, A. Alsalme, A. Alghamdi, M. Arivanandhan, R. Jayavel, Surfactant-free synthesis of Nb2O5 nanoparticles anchored graphene nanocomposites with enhanced electrochemical performance for supercapacitor electrodes. Nanomaterials **10**, 160 (2020)
23. R. Thangappan, S. Kalaiselvam, A. Elayaperumal, R. Jayavel, Synthesis of graphene oxide/vanadium pentoxide composite

nanofibers by electrospinning for supercapacitor applications. Solid State Ionics **268**, 321–325 (2014)
24. J. Jayachandiran, M. Arivanandhan, O. Padmaraj, R. Jayavel, D. Nedumaran, Investigation on ozone-sensing characteristics of surface sensitive hybrid rGO/WO3 nanocomposite films at ambient temperature. Adv. Compos. Mater. **3**, 16–30 (2020)
25. P. Sivasamy, S. Harikrishnan, R. Jayavel, S.I. Hussain, S. Kalaiselvam, L. Lu, Preparation and thermal characteristics of caprylic acid based composite as phase change material for thermal energy storage. Mater. Res. Express. **6**, 105051 (2019)
26. R. Rajendran, L.K. Shrestha, K. Minami, M. Subramanian, R. Jayavel, K. Ariga, Dimensionally integrated nanoarchitectonics for a novel composite from 0D, 1D, and 2D nanomaterials: RGO/CNT/CeO2 ternary nanocomposites with electrochemical performance. J. Mater. Chem. A **2**, 18480–18487 (2014)
27. R. Rajendran, L.K. Shrestha, R.M. Kumar, R. Jayavel, J.P. Hill, K. Ariga, Composite nanoarchitectonics for ternary systems of reduced graphene oxide/carbon nanotubes/nickel oxide with enhanced electrochemical capacitor performance. J. Inorg. Organomet. Polym. Mater. **25**, 267–274 (2015)
28. C. Sengottaiyan, R. Jayavel, R.G. Shrestha, J.P. Hill, K. Ariga, L.K. Shrestha, Electrochemical supercapacitance properties of reduced graphene oxide/Mn2O3:Co3O4 nanocomposite. J. Inorg. Organomet. Polym. Mater. **27**, 576–585 (2017)
29. C. Sengottaiyan, R. Jayavel, R.G. Shrestha, T. Subramani, S. Maji, J.H. Kim, J.P. Hill, K. Ariga, L.K. Shrestha, Indium oxide/carbon nanotube/reduced graphene oxide ternary nanocomposite with enhanced electrochemical supercapacitance. Bull. Chem. Soc. Jpn. **92**, 521–528 (2019)
30. D. Selvakumar, H. Sivaram, A. Alsalme, A. Alghamdi, R. Jayavel, Facile synthesize of free standing highly conducting flexible reduced graphene oxide paper. J. Mater. Sci. Mater. Electron. **27**, 6232–6241 (2016)
31. M. Murugan, R.M. Kumar, A. Alsalme, A. Alghamdi, R. Jayavell, In situ hydrothermal synthesis of graphene-CuO nanocomposites for lithium battery applications. J. Nanosci. Nanotechnol. **16**, 317–320 (2016)
32. D. Selvakumar, A. Alsalme, A. Alghamdi, R. Jayavel, Reduced graphene oxide paper as bimorphic electrical actuators. Mater. Lett. **191**, 182–185 (2017)
33. D. Selvakumar, A. Alsalme, A. Alswieleh, R. Jayavel, Freestanding flexible nitrogen doped-reduced graphene oxide film as an efficient electrode material for solid-state supercapacitors. J. Alloys Compd. **723**, 995–1000 (2017)
34. D. Selvakumar, G. Murugadoss, A. Alsalme, A.M. Alkathiri, R. Jayavel, Heteroatom doped reduced graphene oxide paper for large area perovskite solar cells. Sol. Energy **163**, 564–569 (2018)
35. D. Selvakumar, H. Sivaram, A. Alsalme, A. Alghamdi, R. Jayavel, Freestanding flexible, pure and composite form of reduced graphene oxide paper for ammonia vapor sensing. Sci. Rep. **9**, 8749 (2019)